Acta Materialia 278 (2024) 120229

Contents lists available at ScienceDirect

Acta Materialia

journal homepage: www.elsevier.com/locate/actamat

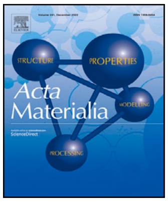

Full length article

Grain boundary diffusion and segregation of Cr in Ni $\Sigma 11(\bar{1}13)[110]$ bicrystals: Decoding the role of grain boundary defects

Shraddha V. Sevlikar [a], G. Mohan Muralikrishna [a], Daniel Gaertner [a], Sergei Starikov [b], Tobias Brink [c], Daniel Scheiber [d], Daria Smirnova [c], Daniel Irmer [e], Bengü Tas [a], Vladimir A. Esin [e,f], Vsevolod I. Razumovskiy [d], Christian H. Liebscher [c,g], Gerhard Wilde [a], Sergiy V. Divinski [a,*]

[a] Institute of Materials Physics, University of Münster, Wilhelm-Klemm-Str. 10, 48149 Münster, Germany
[b] ICAMS, Ruhr-Universität Bochum, Universitätsstraße 150, 44801 Bochum, Germany
[c] Max Planck Institute for Sustainable Materials, Max-Planck-Straße 1, 40237 Düsseldorf, Germany
[d] Materials Center Leoben Forschung GmbH, Roseggerstrasse 12, 8700 Leoben, Austria
[e] Mines Paris, PSL University, Centre des Matériaux (CNRS UMR 7633), Évry, France
[f] Université de Lorraine, CNRS, Institut Jean Lamour, 54000 Nancy, France
[g] RC FEMS & Faculty of Physics and Astronomy, Ruhr University Bochum, Universitätsstraße 150, 44801 Bochum, Germany

ARTICLE INFO

Keywords:
Nickel
Grain boundary diffusion
$\Sigma 11[110]$ boundaries
Segregation
Radiotracer diffusion
DFT calculations
Atomistic simulation

ABSTRACT

Grain boundary diffusion of Cr in a near $\Sigma 11(\bar{1}13)[110]$ Ni bicrystal is measured over a temperature interval between 503 K and 1203 K using the radiotracer technique. The grain boundary diffusion coefficients, D_{gb}, and the triple products, $P = s \cdot \delta \cdot D_{\mathrm{gb}}$, are determined in the C- and B-type kinetics regimes, respectively, with s being the segregation factor and δ the grain boundary width. Opposite to expectations, two distinct contributions to short-circuit diffusion along the nominally single interface are distinguished and related to the existence of two macroscopic facets with distinct grain boundary inclinations and, as a result, distinct structures. The experimental results indicate that the segregation factor of Cr in Ni is about unity, which is fully supported by *ab initio* calculations. Using classical atomistic simulations, Ni grain boundary self-diffusion coefficients are calculated for the symmetric and asymmetric facets. The computational simulations reveal accelerated self-diffusion kinetics along the asymmetric facet, attributing this phenomenon to the presence of disconnection-like defects. This elucidates the experimentally observed diffusion dynamics of chromium atoms, thereby corroborating the heterogeneous mechanisms governing atomic migration across distinct facets.

1. Introduction

Ni–Cr and Ni–Cr–Fe-based alloys are used in various industrial applications over a wide range of temperatures starting at about 550 K for nuclear components up to more than 1300 K for aeronautical applications due to their good oxidation resistance and excellent mechanical properties at high temperatures [1–3]. It is well known that the presence of Cr enhances the oxidation resistance by forming a thin layer of chromium oxide at the surface, which protects the material from further oxidation [4–6].

However, in highly corrosive atmospheres (e.g., hydrogenated water in the temperature range of 573–623 K), these alloys are susceptible to stress corrosion cracking and intergranular crack initiation, which may lead to an early failure of the engineering components. The selective oxidation of Cr-depleted areas predominantly at the crack tips plays a major role in the propagation of the stress corrosion-driven cracks [7,8]. Many of these processes are controlled by diffusion in the vicinity of grain boundaries.

Grain boundaries (GB) are planar defects in a crystalline material that separate differently oriented grains [9]. They exhibit a higher number of crystallographic degrees of freedom compared to the bulk crystal. Depending on specific structures, GBs possess an excess free volume (compared to the bulk), facilitate GB sliding during creep [9] and are typically preferred diffusion pathways in a polycrystalline material [10]. Grain boundaries play an important role in processes such as recrystallization, grain growth, sintering, segregation and stress corrosion cracking [11,12]. They can also act as sites for heterogeneous nucleation during phase transformations [12,13]. The properties of GBs can be controlled through appropriate thermo-mechanical treatment

---

* Corresponding author.
E-mail address: divin@uni-muenster.de (S.V. Divinski).

https://doi.org/10.1016/j.actamat.2024.120229
Received 17 May 2024; Received in revised form 10 July 2024; Accepted 26 July 2024

and/or by applying specific solidification routes [14]. Atomic transport along GBs must be taken into account in phase transformations and deformation processes, especially at high temperatures [15–17]. Using radiotracer diffusion measurements, the existence of structural GB phase transitions was discovered [18,19] and they have become a subject of intensive studies [20–23].

GB diffusion of Ni and Cr in polycrystalline pure Ni and Ni–Cr based alloys was already investigated at high temperatures [24,25], but studies at low temperatures ($T < 873$ K) are rare [26].

So far, all studies on Cr GB diffusion in Ni or Ni-based alloys were concentrated on polycrystalline materials and the kinetic properties of general (random) high-angle GBs were addressed [24,26]. Investigations on bicrystals are more fundamental and could provide basic information on the structure–property relations, as it was found, e.g., for solute GB diffusion in Al [27–31], Cu [18,32–35] or Ag [36,37] bicrystals. In Ni bicrystals, GB diffusion was measured only for selected low-angle tilt and twist boundaries [38]. Diffusion measurements on a single grain boundary provide a sensitive probe to structural and compositional changes of GBs, though they are challenging with respect to the demands to detect low concentrations of the diffusing element, especially at low temperatures [39].

The present paper is focused on radiotracer measurements of Cr GB diffusion and segregation in near $\Sigma 11(\bar{1}13)[110]$ Ni bicrystals. The use of bicrystals allows one to experimentally investigate diffusion along a single grain boundary with a presumably well defined structure, serving as a basis for establishing a quantitative correlation with density functional theory (DFT)-based calculations and atomistic simulations using empirical interatomic potentials. Such combination of radiotracer measurements and DFT calculations enabled an accurate estimation of Cr segregation and GB diffusion kinetics.

The present experimental measurements are fully supported by zero-Kelvin DFT calculations of interface structure and the Cr segregation at different GB sites. Furthermore, molecular dynamics (MD) calculations with empirical interatomic potentials are employed to examine the propensity of the $\Sigma 11(\bar{1}13)[110]$ interface in Ni to structural transitions at elevated temperatures and analyze the impact of GB inclination, i.e. the deviation from the perfectly symmetric boundary, on GB self-diffusion. Finally, *large-scale* MD simulations were used to investigate the atomistic structure of the asymmetric $\Sigma 11[110]$ GBs that allowed an adequate explanation of the experimental findings. The employed cross-scale experimental–atomistic MD–ab initio Ansatz revealed a unique contribution of disconnection-like defects of GB structures and their role in atomic transport.

2. Methodology

2.1. Sample preparation

Ni bicrystals were fabricated by a modified Bridgman technique using high-purity (99.999 wt%) ingots. Single crystalline seeds were carefully oriented to obtain a common [110] tilt axis for the two crystals and a nearly perfect symmetric $(\bar{1}13)$ GB plane.

The grown Ni bicrystals were cut into discs with a thickness of approximately 1 mm by spark erosion and were mechanically polished using a standard metallographic procedure in order to achieve a mirror-like surface finish. These discs were pre-annealed at 518 K for 4 h and subsequently at 1211 K for 16 h in an evacuated quartz tube filled with high purity (5N) argon for stress relaxation. Subsequently, the samples were annealed at the temperatures and for the times of the intended GB diffusion measurements to produce equilibrated structures, including equilibrium segregation of spurious impurities.

2.2. Microstructure characterization

The samples for microstructural analyses were prepared by standard mechanical polishing with abrasive SiC papers down to 5 μm grid size, following by grinding using 3 and 1 μm diamond suspensions and finally using an OP-S suspension.

The bicrystal quality and crystallography of the GB plane were investigated by electron back-scatter diffraction (EBSD) using a scanning electron microscope (SEM, FEI Nova Nano SEM 230) at an acceleration voltage of 20 kV. The tilt angle and the working distance were fixed at 70° and 15 mm, respectively. The clean-up process to neighboring CI over 0.2 was performed after the EBSD maps were measured. Typically, a step size of 200 nm was used.

A 3D-EBSD investigation was performed using successive plane parallel sectioning by grinding with the determination of the EBSD maps for each section. The plane coordinates (x, z) in different sections were aligned using the micro-indents of known geometry as markers that were placed along the GB on both sides at reasonable distances from the interface. The depth coordinate y was determined by weighing the sample of known geometry and density before and after each grinding step on a micro-balance (accuracy of about ± 0.1 μg).

2.3. Radiotracer experiments

The radioisotope ^{51}Cr (half-life of 27.7 days) was used in the form of a highly diluted HCl solution. The original tracer solution was further diluted with double-distilled water in order to achieve the required specific activity of the tracer material. The radioactive solution was deposited using a drop-and-dry technique and the samples were sealed in an evacuated quartz tube filled with high purity (5N) argon. The diffusion annealing treatments were performed in the temperature interval of 503 K–1303 K. The temperature of the furnace was continuously measured using a Ni-NiCr thermocouple with an accuracy of ±1 K.

The diameter of the diffusion-annealed samples was reduced by at least 0.5 mm (the exact value was larger than the bulk diffusion length $\sqrt{D_v t}$ by at least a factor of five) in order to remove the effects of lateral and surface diffusion. Here D_v and t are the volume diffusion coefficient and the diffusion time, respectively.

Subsequently, the samples were sectioned in a plane-parallel manner using a high precision grinding machine [40]. The thickness of each section was determined by measuring the mass difference before and after grinding using a high precision micro-balance. The relative specific activity of each section was measured using an intrinsic Ge detector equipped with a 16 K multi-channel analyzer to count the decays of the ^{51}Cr isotope emitting γ-quanta with an energy of 320 kV [41].

2.4. SIMS measurements

The SIMS measurements were carried out to estimate the bulk diffusion coefficient of Cr in the present Ni material at a relatively low temperature of 873 K to verify the reliability of the extrapolation of the existing bulk diffusion data [42–45] within the whole range of the intended GB diffusion experiments. The Ni bicrystal sample was prepared for the diffusion study according to the procedure detailed in Ref. [40]. At first, the sample was subjected to the heat treatment at the temperature of diffusion annealing for three times the duration of the actual diffusion experiment to achieve equilibrium conditions. The heat treated sample was carefully polished and subsequently a 5 nm thick layer of natural Cr was deposited and subjected to the diffusion annealing at 873 K for 15 h inside an evacuated and sealed quartz tube to avoid oxidation while annealing.

SIMS measurements were carried out using a Cameca IMS 7f apparatus and a duo plasmatron $(O_2)^+$ source. Primary ion beam current and energy were set to 50 nA and 5 keV, respectively. The sputtered area was 150 μm^2. This area was carefully selected to be reasonably far from the grain boundary in order to provide reliable volume diffusion data. To minimize roughening during the sputtering, the chamber was purged with a small pressure of oxygen. The isotopes ^{12}C, ^{16}O, ^{50}Cr, ^{52}Cr, ^{54}Cr, ^{56}Fe, ^{58}Ni, ^{60}Ni, ^{64}Ni were recorded. The sputtering rate (and therefore sputtering depth) was estimated by measuring the crater depths after sputtering using a Dektak 8 contact profilometer manufactured by Bruker. After straightening of the signal, the depth was measured as the height difference between the average height in the crater center and the sample surface. For each crater, three profiles were measured and the average value of the three profiles was considered as the final crater depth.

2.5. *Atomistic simulations with empirical interatomic potentials*

We performed molecular dynamics (MD) and molecular statics computer simulations to both find possible grain boundary structures on an atomic level and to study the resulting self-diffusion in these structures. We used LAMMPS [46,47] with an embedded atom method (EAM) potential for Ni [48]. Additional testing of the stability of the GB structure at high temperatures was also carried out with an earlier version of this EAM potential [49]. Some calculations with respect to Cr segregation at Ni GBs were performed using the angular-dependent potential (ADP) for the Ni–Cr system [50].

2.5.1. *Grain boundary structure*

Grain boundaries can exhibit different microstates, even for the same macroscopic, bicrystallographic parameters [21,51–57]. These microstates can influence segregation [58–60] and/or diffusion [18, 19]. They can be treated thermodynamically as equivalents to bulk phases [61,62] and are called GB phases [56] or complexions [21,54, 55].

We sampled the possible complexions of the $\Sigma 11$ GB by molecular statics simulations. Two fcc crystallites were created with $(\bar{3}\bar{3}2)$, (113), $(\bar{1}10)$ and $(\overline{332})$, $(\bar{1}\bar{1}3)$, $(\bar{1}10)$ surfaces, respectively, and joined along the y direction to produce a $\Sigma 11(\bar{1}13)[110]$ tilt grain boundary. The resulting unit cell has a size of approximately $8.255 \times 160 \times 2.489$ $\mathring{A}^3$ and contains 264 atoms. Periodic boundary conditions were applied along x and z (tilt axis direction and parallel to the grain boundary), while the y direction (normal to the grain boundary) had open surfaces. This unit cell was repeated from 1 to 5 times in the x direction and from 1 to 3 times in the z direction (different supercells were generated). To sample the possible states, we applied 121 different relative displacements between the crystallites (within the xz plane) and minimized the potential energy of the system (the γ-surface method [63]).

It is known that this procedure by itself is still insufficient to find all possible structures, because instead of joining two fully occupied crystallographic planes at the GB, it is also possible that low-energy GBs result from the joining of partially occupied planes [20,64]. We therefore repeated these simulations, but introduced GB vacancies by randomly removing atoms in the GB. If there are N_{GB} atoms in the designated GB region, we systematically sampled the removal of 1, 2, …, $N_{\mathrm{GB}} - 1$ atoms for all displacements and supercells.

In addition to this search at $T = 0$ K, we also performed MD simulations at an elevated temperature to see if additional high-temperature complexions occurred. We chose an annealing temperature of 1400 K, as a temperature that is high enough to enable diffusion and complexion transitions within the MD timescale, but which is low enough to avoid GB premelting/disordering. We ran simulations for 30 ns on a system of size $500 \times 190 \times 50$ $\mathring{A}^3$ (422,400 atoms) with open boundaries in x and y direction and a barostat at ambient pressure in z direction. The open boundaries enable diffusion-controlled complexion transitions [20]. For these simulations, we both started from the low-energy $\Sigma 11$ structure found using the molecular statics sampling, and from a structure with 1200 vacancies introduced in the GB region (cf. Ref. [20]). To verify the obtained results, we repeated these simulations with an older EAM potential [49], which yielded equivalent results, but which will only be discussed where relevant later.

2.5.2. *Diffusion simulations*

We studied the diffusion process on the atomistic scale for the experimentally relevant GB configurations. The simulations were carried out only for Ni diffusion (i.e. self-diffusion). However, it can be expected that the calculated characteristics should be close to the characteristics of Cr diffusion, since the segregation factor is almost equal to unity, as it was found by DFT calculations, see Section 3.5.2 below. Diffusion calculations for Cr atoms (in the dilute limit) using the existing Ni–Cr potential [50] were not performed, since such a study would be highly expensive in terms of the computation time.

The investigation was divided into two parts: (1) study of the diffusion characteristics of a single vacancy and (2) large-scale atomistic simulation of self-diffusion in the spirit of a numerical experiment.

Several finite-temperature MD simulations were performed to calculate the volume diffusion coefficients for a single vacancy D_{v}^{vac}. A computational box consisted of 499 Ni atoms arranged in a fcc lattice with one empty site. Each calculation was carried out in the NPT ensemble to maintain zero pressure and temperature T. The diffusion coefficients were extracted from the sum of the squared displacements (δr_i^2) of all N atoms in the simulated system during the calculation time t,

$$D_{\mathrm{v}}^{vac} = \sum_{i=1}^{N} \delta r_i^2 / 6t. \tag{1}$$

We found that MD time-length $t = 20$ ns is sufficient for a reliable determination of D_{v}^{vac}. To study the vacancy diffusion coefficients in $\Sigma 11(\bar{1}13)[110]$ tilt GB, similar MD calculations were performed for a simulation cell containing two GBs and a single vacancy within one of them. The simulated system consisted of 30375 atoms and had periodic boundary conditions. The diffusion coefficients D_{gb}^{vac} were estimated from the displacements of atoms in the GB region with a thickness of $\delta = 1$ nm. It should be noted that the typical value of δ when analyzing experimental data is usually taken to be 0.5 nm. In our simulation, we used the value of 1 nm to capture the entire vacancy trajectory near the GB. For this calculation, only displacements along the tilt axis z were taken into account: $D_{\mathrm{gb}}^{vac} = \sum \delta z_i^2 / (2t)$

The calculated vacancy diffusion coefficients were "converted" into the self-diffusion coefficients (D_{v} and D_{gb}) by multiplying by the vacancy concentration:

$$D_{\mathrm{v}} = D_{\mathrm{v}}^{vac} \cdot \exp\left[(TS^{vac} - E_{\mathrm{v}}^{vac})/k_B T\right] \tag{2}$$

and

$$D_{\mathrm{gb}} = D_{\mathrm{gb}}^{vac} \cdot \eta \cdot \exp\left[(TS^{vac} - E_{\mathrm{gb}}^{vac})/k_B T\right] \tag{3}$$

where k_B is the Boltzmann constant and $S^{vac} = 2k_B$ is the vacancy formation entropy [65,66]. The formation energies of a vacancy for volume and GB cases (E_{v}^{vac} and E_{gb}^{vac}) were calculated with the static calculations similar to recent works [67,68]. The fitting parameter η was used to account for the diversity of different energy/entropy values of vacancy sites near the GB. We obtained $\eta = 0.16$ by comparing D_{gb} estimated from Eq. (3) with the results of the large-scale direct MD simulation.

In large-scale modeling, the GB diffusion coefficients were calculated from the direct MD simulation of average atomic displacements in spherical nanoparticles containing two grains. The similar method was used recently to calculate GB self-diffusion coefficients in Fe [67] and Nb [68]. Following the experimental findings, two different types of GBs were simulated: (1) perfect (symmetric) $\Sigma 11(\bar{1}13)[110]$ GB and (2) asymmetric GBs with the same misorientation but with an inclination angle of 15°. The applied inclination is larger than in the experimental part, but the value of the inclination angle mainly affects the density of linear defects (fast diffusion channels), which are the subject of the study (see below). The simulated nanoparticles consisted of 459330 atoms. The large-scale simulation involves two consecutive stages: an annealing stage and a main MD run. The annealing stage is necessary

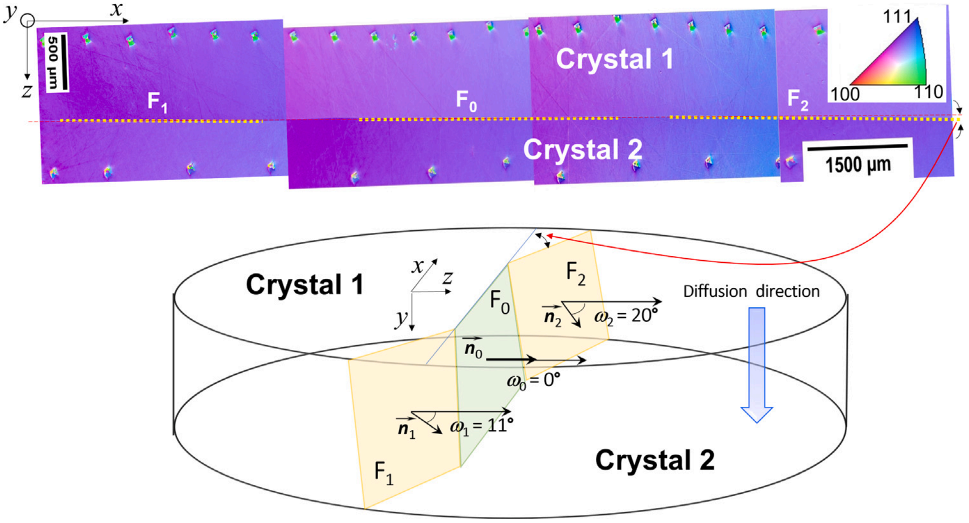

Fig. 1. (upper panel) EBSD image of the sample surface with indicated macroscopic facets (yellow dotted lines) of the interface between the two grains (noted Crystal 1 and Crystal 2). The microindents are used for exact determination of the GB inclination via serial sectioning by mechanical grinding. Note that the image is stretched to represent the whole sample. The crystallographic orientations of planes parallel to the sample surface are color coded according to the inverse pole figure map shown as insert. Three facets, F_0, F_1, and F_2 are identified and the horizontal red line shows the orientation of the central facet F_0. The traces of the facets F_1 and F_2 are slightly inclined with respect to F_0 at about 3°. (bottom panel) Schematic (without keeping the right proportions to highlight the inclinations) visualization of the GB plane in the Ni bicrystal with a central symmetric facet F_0 with the normal vector $\vec{n}_0$ perpendicular to the sample surface, and two outer asymmetric facets, F_1 and F_2, with the normal vectors $\vec{n}_1$ and $\vec{n}_2$ inclined with respect to $\vec{n}_0$. The angles ω_i measure the deviations of the facets from the symmetric orientation. The diffusion direction is indicated (along the y axis).

to achieve the equilibrium concentration of point defects inside a GB. The performed annealing time was 2 ns. The diffusion coefficients $D_{\rm gb}$ were estimated from the main MD run, which was set to be two times longer than the annealing stage. The value of $D_{\rm gb}$ was calculated as $\sum \delta z_i^2/(2tN_{gb})$, where the summation was performed over all atoms in the GB region N_{gb}. The thickness of the GB region was 1 nm and 1.5 nm for symmetric and asymmetric facets, respectively (the difference in thickness is due to a more complex structure of the asymmetric facet).

2.6. *Ab initio calculations of Cr GB segregation*

The first principles calculations were conducted using the Vienna Ab Initio Simulation Package (VASP) [69–72] using the projector-augmented wavefunctions (PAW) framework [72,73]. The system was modeled with spin-polarization to allow for magnetic moments on all atoms. We chose the Perdew–Burke–Ernzerhof (PBE) [74] flavor of the GGA xc-functionals as these are known to well reproduce bulk properties of Ni [75]. The energy cutoff was set to 400 eV and the k-point density was chosen as 40 Å^{-1}. The force criterion for the ionic relaxations was set to 9×10^{-3} eV/Å. These settings converged the segregation to 0.01 eV/atom and lead to a lattice parameter of 3.515 Å in good agreement with experiment [75].

The GB energies are computed as

$$\gamma_{\rm gb} = \frac{E_{\rm gb} - E_{slab}}{A}, \tag{4}$$

with $E_{\rm gb}$ and E_{slab} are total energies of the GB cell and a slab cell with the same number of atoms but no GB defect inside, respectively, where A corresponds to the area of the GB. The GB segregation energy was calculated from GB slabs and a bulk reference using [76]

$$E_{seg} = (E^{Cr}_{\rm gb} - E_{\rm gb}) - (E^{Cr}_{Bulk} - E_{Bulk}). \tag{5}$$

Here, $E_{\rm gb}$ and $E^{Cr}_{\rm gb}$ denote the pure and the Cr decorated GB simulation slabs, whereas E_{Bulk} and E^{Cr}_{Bulk} correspond to the bulk reference structures without and with a Cr atom. The bulk reference structure is a cubic fcc cell with 256 atoms. For the GB slabs, the CSL GBs $\Sigma5(012)[100]$ and $\Sigma11(\bar{1}13)[110]$, where the latter was selected in accordance to the observed structure in the bicrystal. Both GB structures contain 76 atoms and a vacuum layer on top to allow for GB relaxations normal to the GB plane. While the $\Sigma5$ GB has a relatively open structure corresponding to high energy GBs, the $\Sigma11$ GB has an atomic coordination closer to the bulk fcc with a relatively low energy.

3. Results and discussion

3.1. *Microstructure characterization*

Since GB diffusion and segregation depend on the crystallographic parameters of the interface [12], including both the grain misorientation [33] and/or the boundary inclination [77], we performed a careful 3D-EBSD examination of the Ni bicrystal.

A panoramic view composed of a series of EBSD images of the whole surface of the Ni bicrystal is shown in Fig. 1(a), that substantiates the existence of two grains with an average misorientation of 49.6° ± 3° corresponding to a $\Sigma11[110]$ grain boundary and the GB plane near $(\bar{1}13)$. Though, a very careful inspection reveals that the GB plane does not intersect the sample surface along a straight line and several macroscopic segments are seen, indicated by yellow dotted lines in Fig. 1 (upper panel). On the sample surface, the side facets are inclined with respect to the central one at about 3°. This inclination is highlighted as deflections of the outer yellow lines for the facets F_1 and F_2 with respect to the orientation of the central facet F_0, which corresponds to the symmetric GB with the boundary parallel to the $(\bar{1}13)$ crystallographic plane, thin red line in Fig. 1 (upper panel). The diffusion direction, which is normal to the sample surface, is found to be almost perpendicular to the determined tilt axis [110].

The results of a 3D-EBSD study are schematically shown in Fig. 1 (bottom panel). Two types of macroscopic segments are identified. The central one, F_0, represents a symmetric $\Sigma11(\bar{1}13)[110]$ GB facet with the GB plane oriented perpendicularly to the sample surface, i.e. parallel to the macroscopic diffusion direction in the radiotracer measurements. The two outer segments correspond to the asymmetric facets F_1 and F_2 with the GB plane inclined totally at about $11° \pm 1°$ (F_1) or $20° \pm 1°$ (F_2) with respect to the symmetric plane. The corresponding inclination angles ω_1 and ω_2 are shown in Fig. 1(b) as angles between the normal directions to the GB segments, $\vec{n}_1$ and $\vec{n}_2$, and that direction for the symmetric facet. The GB planes for the facets F_1 and F_2 were found to correspond approximately to the $(\overline{3}\overline{3}2)$ and $(\overline{8}\overline{5}3)$ crystallographic planes, respectively.

This specific shape of the grain boundary in the Ni bicrystal was checked to remain unchanged after annealing treatments mimicking the diffusion measurements.

3.2. Volume diffusion

3.2.1. SIMS analysis of Cr volume diffusion

Reliable volume diffusion data are imperative for a correct analysis of GB diffusion. Cr bulk diffusion in pure Ni was measured by Monma et a. [42], Růžičková and Million [43], Jung et al. [44], and by Gheno et al. [45]. To provide precise data on Cr GB diffusion, especially at lower temperatures of the intended GB diffusion measurements, we re-examined Cr bulk diffusion in the present Ni material to take into account a potential impact of spurious impurities present in the bicrystalline material.

The raw data obtained by SIMS were analyzed using the procedure described in Ref. [40]. For both diffusion samples (after diffusion annealing at 873 K for 15 h) and the reference sample (without annealing to obtain the so-called “zero-profile”), only the data obtained at depths after stabilization of the ^{16}O signal was completed, corresponding to the stationary regime, were used. The signal of ^{52}Cr, the most abundant Cr isotope, was normalized by the signal of ^{64}Ni, to avoid a difference of the obtained data due to ion beam intensity and crater size variation from one crater to another and to be able to compare thus the data from different craters. After the subtraction of the zero profile data, the obtained concentration profiles of Cr diffusion were fitted using the solution of Fick’s second law for a constant source and a semi-infinite sample,

$$c(y,t) = c_S + (c_0 - c_S)\,\mathrm{erf}\left(\frac{y - y_0}{2\sqrt{D_\mathrm{v} t}}\right), \tag{6}$$

where c_0 is the background level, the c_S is the experimental signal given with respect to the reference coordinate y_0. Although a relatively small thickness of the natural Cr layer was deposited on the sample surface, the constant source conditions held in the present conditions of diffusion at 873 K. Moreover, pure Cr was still observed on the sample surface after the diffusion experiment. As a result, only a relatively small fraction of the applied Cr atoms diffused in the sample. The relatively large penetration depth of about 100 nm has not to be misleading, since the SIMS signal represents a relative intensity, which is proportional to the Cr concentration.

The concentration profile measured by SIMS and analyzed using Eq. (6) is presented in Fig. 2.

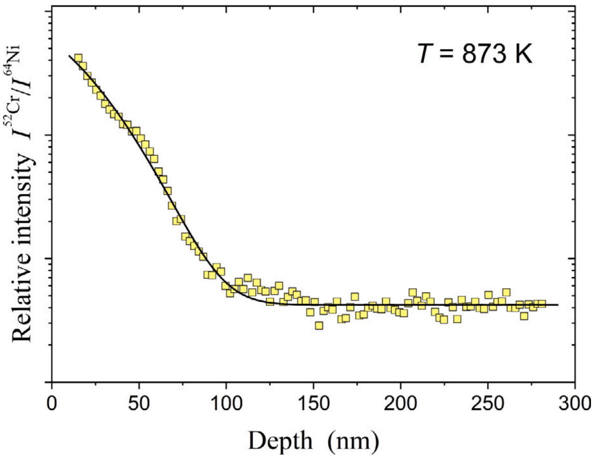

Fig. 2. Concentration profiles of ^{52}Cr bulk diffusion in Ni at 873 K for 15 h measured by SIMS. The solid line represents the fit according to Eq. (6).

An analysis of the combined literature [42–45] and the present data results in the following temperature dependence of Cr volume diffusion in pure Ni in the temperature interval of 815 K ≤ T ≤ 1573 K (Fig. 3),

$$\begin{aligned} D_\mathrm{v}^\mathrm{Cr} &= \left(1.99^{+0.62}_{-0.47}\right) 10^{-5} \\ &\times \exp\left(-\frac{(276.6 \pm 3.0)\ \mathrm{kJ/mol}}{RT}\right)\ \mathrm{m^2 s^{-1}} \end{aligned} \tag{7}$$

where R is the universal gas constant and T the absolute temperature. This Arrhenius-type approximation is used in all relevant estimations below. Note that the data points at the temperatures close to the melting point, $T > 1573$ K, are not included in the fit due to expected anharmonic contributions [66], similarly to other fcc metals [79].

Fig. 3 substantiates that volume diffusion of Cr in Ni is consistently measured and Eq. (7) can be used for a reliable analysis of GB diffusion data, including moderate and even lower temperatures.

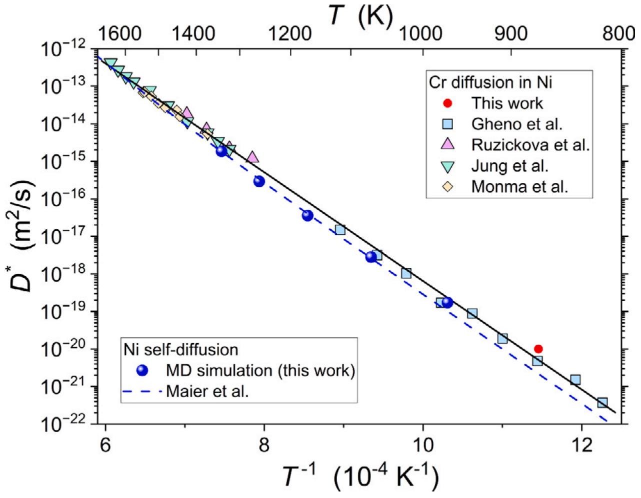

Fig. 3. The present data (red circle) for volume diffusion of Cr in pure Ni in comparison with the literature data of Gheno et al. [45] (squares), Jung et al. [44] (triangles down), Monma et al. [42] (diamonds), et al. [43] (triangles up). The black solid line represents the common Arrhenius-type fit to the complete data set according to Eq. (7). The experimentally measured Ni self-diffusion data reported by Maier et al. [78] (blue dashed line) are shown for comparison with the present results of MD simulation (blue spheres). (For interpretation of the references to color in this figure legend, the reader is referred to the web version of this article.)

3.2.2. Atomistic study of Ni self-diffusion

In order to test the performance of the used inter-atomic potentials and the developed calculation scheme, Ni volume self-diffusion was simulated first. Since the available Ni–Cr interatomic potentials [50] was not yet tested for GB structures and diffusion calculations, we focused on Ni self-diffusion using a reliable and extensively utilized EAM potential [48].

In Fig. 3, the MD simulation results for the volume self-diffusion coefficients are shown. The vacancy concentration was estimated with the formation energy $E_v^{vac} = 1.57$ eV obtained in the static calculations. The calculated values are in perfect agreement with the experimentally measured Ni self-diffusion data [78]. Furthermore, the Ni self-diffusion rates are close to the measured Cr diffusion coefficients, Fig. 3. The similarity of the Ni self-diffusion and Cr diffusion coefficients was also confirmed in various experimental works [43,78].

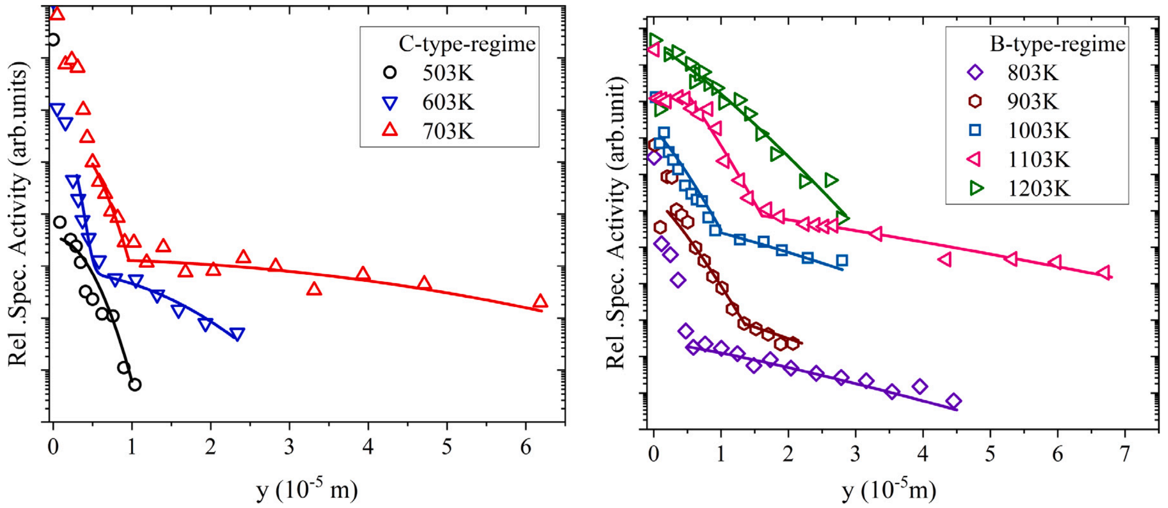

Fig. 4. The penetration profiles of Cr diffusion in Ni bicrystals in the C-type (a) and B-type (b) kinetic regimes. y is the penetration depth.

Table 1
Experimental conditions (temperature T and time t) and the determined diffusion parameters of the radiotracer experiments (the parameters α and β are defined by Eqs. (8) and (16), respectively). The uncertainty of the D_{gb} values is typically below 20%, if not explicitly specified. Kinetic regimes of GB diffusion are specified.

T K	t 10^4 s	$\sqrt{D_{\mathrm{v}}t}$ 10^{-6} m	D_{gb}^{slow} 10^{-17} m^2 s^{-1}	D_{gb}^{fast} 10^{-16} m^2 s^{-1}	P^{slow} 10^{-23} m^3 s^{-1}	P^{fast} 10^{-22} m^3 s^{-1}	α	β^{slow}	β^{fast}	f^{slow}	Regime
503	86.4	9.99×10^{-8}	–	0.0456	–	–	2.5×10^3	–	–	–	C
603	25.9	1.11×10^{-5}	0.27	1.49	–	–	2.3×10^1	–	–	0.99	C
703	25.9	4.95×10^{-4}	1.58	15.8	–	–	5.0×10^{-1}	–	–	0.97	BC
803	25.9	8.59×10^{-3}	–	–	–	0.0655	2.9×10^{-2}	–	1.3×10^6	–	B
903[a]	25.9	7.92×10^{-2}	–	–	0.219	0.363	3.2×10^{-3}	570	9.5×10^3	0.99	B
1003	25.9	0.469	–	–	1.12	2.57	5.3×10^{-4}	14	320	0.96	B
1103	25.9	2.01	–	–	4.52	30.2	1.3×10^{-4}	0.73	49	0.99	B
1203	1.08	1.38	–	–	–	23.7	1.8×10^{-4}	–	4.9	–	B

[a] The uncertainty of the determined value of P^{fast} is large, up to +46% and −82% due to a relatively short branch relevant for the corresponding contribution.

3.3. Radiotracer GB diffusion measurements

The way to analyze the grain boundary penetration profiles crucially depends on the kinetic regime in which the measurements are performed. The key parameter is the value of the Le Claire parameter α [80],

$$\alpha = \frac{s\delta}{2\sqrt{D_{\mathrm{v}}t}}, \tag{8}$$

relating GB segregation factor and the effective grain boundary width, $s \cdot \delta$, with the corresponding bulk diffusion length in the grain. Generally, α is unknown for solute diffusion due to the segregation factor s, which is unknown a priori. δ is the GB width measured to be 0.5 nm [25,81].

The SIMS measurements of Cr diffusion in poly-crystalline high purity (5N) Ni indicate a segregation factor of about unity [26]. This behavior will be confirmed by the present experiments and the theoretical analysis, see Section 3.5.2 below. Therefore, the grain boundary diffusion regimes can directly be established 'on demand' by a proper choice of the annealing time t at the given temperature T. According to the present knowledge [82], the grain-boundary diffusion corresponds to Harrison's C-type regime (lower temperatures and/or shorter diffusion times) if the Le Claire parameter α is larger than 1 and the B-type condition (higher temperatures and/or longer diffusion times) is satisfied if $\alpha < 0.1$. An interval of $0.1 < \alpha < 1$ represents the transition regime BC (for a theoretical estimate of the limits of diffusion regimes see also Ref. [83]).

In order to analyze the grain boundary diffusion kinetics and the penetration profiles in the B-type regime, the volume diffusion coefficients of Cr in Ni assessed by Eq. (7) are used.

3.3.1. C-type diffusion regime

In Fig. 4(a), the concentration profiles measured under the C-type regime conditions are shown. The profiles measured at 603 K and 703 K reveal unexpectedly two distinct contributions that follow the shape predicted by the Gaussian solution of the diffusion problem (the logarithm of the tracer concentration decreases linearly with the penetration depth squared),

$$\bar{c} = A^{slow} \exp\left(-\frac{y^2}{4D_{\mathrm{gb}}^{slow}t}\right) + A^{fast} \exp\left(-\frac{y^2}{4D_{\mathrm{gb}}^{fast}t}\right). \tag{9}$$

Here $\bar{c}$ is the relative specific activity of the layer, which is proportional to the solute concentration, y is the penetration depth, A^{slow} and A^{fast} are the corresponding pre-factors and D_{gb}^{slow} and D_{gb}^{fast} are the pertinent diffusion coefficients. At $T = 503$ K, only one branch, presumably the "fast" contribution, was reliably resolved.

Since a consistent classification of the contributions in terms of specific segments is not straightforward and can be done in a self-consistent manner only after an analysis of the complete diffusion data set, Section 3.4, we are first distinguishing them as relatively "slow" (near surface, steeper branch) and relatively "fast" (deeper, shallower branch) branches. This simple classification facilitates a correct processing of the experimental profiles at any given temperature.

In this way, two grain boundary diffusion coefficients, D_{gb}^{slow} (D_{gb}^{fast}), are determined as

$$D_{\mathrm{gb}}^{slow} = \frac{1}{4t}\left(-\frac{\partial \ln \bar{c}}{\partial y^2}\right), \tag{10}$$

using the "short" penetration depths (and similarly for D_{gb}^{fast} using the "long" penetration depths).

Such a shape of the penetration profiles was frequently observed during the GB diffusion measurements on polycrystalline materials and a number of factors may potentially induce two distinct GB diffusion-related branches [82]:

(i) a hierarchy of short-circuits in the material, i.e. a co-existence of different types of GBs, like low-angle and high-angle GBs [84] or nano-crystalline GBs and interfaces between clusters of these nano-grains [85,86];
(ii) GB motion during diffusion annealing [87–89];
(iii) non-linear segregation of the diffusing element (solute) at the GBs [90,91].

Cases (i) and (ii) are not relevant in the present investigation since we are studying diffusion in a single stationary boundary.[1] The curved concentration profiles can correspond to a non-linear segregation in a single GB [91] under the B-type diffusion regime only, since the solute segregation does not affect the shape of the penetration profiles measured in the C-type regime.[2] Moreover, we have systematically applied very low amounts of the radiotracer solution to deal with low concentrations of the Cr atoms in the bicrystals. Thus, the reason (iii) can also be ruled out.

Such non-classical shape of the penetration profiles of GB diffusion in a bi-crystalline sample was observed previously [92] and it may be explained by the further factors:

(iv) a structural multiplicity of a single interface as it was proposed by Rabkin et al. [92];
(v) a co-existence of macro-facets with strongly different inclinations which might be characterized by different diffusivities [77].

The latter scenario seems to correspond to the results of the microscopic characterization applying 3D orientation imaging microscopy, Section 3.1. It will be further examined using molecular dynamics (MD) simulations, Sections 3.6 and 3.7, and a diffusion analysis, Eqs. (11)–(19), see below. As a result, the co-existence of macro-facets with strongly different inclinations, scenario (iv), as a unique reason of the appearance of the two branches in the penetration profiles will be verified, Section 3.1.

The relevant parameters of this diffusion experiment and the determined grain boundary diffusion rates are summarized in Table 1. The value of the parameter α is estimated assuming that the segregation factor $s = 1$. If Cr atoms segregate at the Ni GB, the value of the parameter α would be larger, confirming that the conditions of the C-type regime, $\alpha > 1$, are satisfied.

The derived diffusion data allow estimating the relative fractions of the GB segments (facets) with distinct diffusivities. The pre-factors A^{slow} and A^{fast} can be written as,

$$A^{slow} = \frac{\Omega M f^{slow}}{\sqrt{\pi D_{\rm gb}^{slow} t}} \tag{11}$$

and

$$A^{fast} = \frac{\Omega M f^{fast}}{\sqrt{\pi D_{\rm gb}^{fast} t}}, \tag{12}$$

with $f^{slow} + f^{fast} = 1$. Here f^{slow} (f^{fast}) is the area fraction of the "slow" ("fast") branch of the Ni GB; M is the amount of the deposited radiotracer per unit area of the specimen surface; and Ω is the fraction of the tracer material diffused in the sample via the grain boundary. If surface diffusion is infinitely slow (frozen), Ω can be estimated as $\Omega \approx \delta/L$, where L is the specimen diameter (the GB length on the sample surface). Note that one may introduce a numerical factor in the above relation, and its exact value is determined by the sample geometry. If surface diffusion would be infinitely fast, Ω would approach unity. In reality, Ω attains a value between these two extremes and can be estimated from the magnitude of the drop of the tracer concentration near the sample surface. However, its exact value is not required for the current analysis.

The value of f^{slow} (and correspondingly of f^{fast}, $f^{fast} = 1 - f^{slow}$) can be determined as,

$$\frac{f^{slow}}{1 - f^{slow}} = \frac{A^{slow}}{A^{fast}} \left(\frac{D_{\rm gb}^{slow}}{D_{\rm gb}^{fast}} \right)^{1/2}. \tag{13}$$

The determined values of f^{slow} is given in Table 1.

3.3.2. B-type diffusion regime

The diffusion experiments under the intended B-type regime conditions were performed at five different temperatures in the range of 803 K – 1203 K and the penetration profiles are shown in Fig. 4(b).

According to Le Claire [93], who numerically approximated Suzuoka's exact solution [94] considering the results provided by Levine and MacCallum [95], the grain-boundary related tails of the penetration profile have to be almost linear in the coordinates of $\ln \bar{c}$ against $y^{1.2}$. However, similarly to the case of C-type diffusion, two distinct contributions of short-circuit diffusion are seen at the depths exceeding those affected by volume diffusion, i.e. $y > 5\sqrt{D_{\rm v} t}$, see Table 1. By distinguishing systematically "slow" and "fast" branches, these contributions are approximated as,

$$\bar{c} = B^{slow} \exp\left(-q^{slow} y^{1.2}\right) + B^{fast} \exp\left(-q^{fast} y^{1.2}\right). \tag{14}$$

The pertinent slopes, $q^{slow} = -\partial \ln \bar{c}/\partial y^{1.2}$ or $q^{fast} = -\partial \ln \bar{c}/\partial y^{1.2}$, approximating the corresponding branches of the penetration profile, allow the determination of the values of the triple products [10],

$$P^{slow} = s\delta D_{\rm gb}^{slow} = 1.33 \sqrt{\frac{D_{\rm v}}{t}} \left(q^{slow}\right)^{-5/3} \tag{15}$$

and an equivalent expression for P^{fast}. The exact expression for the triple product is determined by the value of the second Le Claire parameter β, which describes the relation between grain boundary and volume diffusion,

$$\beta^{slow} = \frac{P^{slow}}{2 D_{\rm v} \sqrt{D_{\rm v} t}}. \tag{16}$$

and a similar expression for β^{fast}. The exact expressions for P^{slow} (P^{fast}) as a function of the value of β^{slow} (β^{fast}) are provided by Kaur et al. [10]. In the case of $\beta < 10$, the exact Suzuoka solution [94] was used to derive the corresponding triple product values.

The diffusion parameters and the determined values of the triple products P^{slow} and P^{fast} are summarized in Table 1. At $T = 803$ K only one ("fast") branch was reliably resolved. Only few data points indicate the presence of the "slow" branch at $T = 803$ K, but one cannot derive reliable diffusion data for $D_{\rm gb}^{slow}$ at this temperature.

Following the same interpretation as for the C-type measurements, which will be supported by detailed microscopic observations, Section 3.1, a co-existence of two GB segments is assumed. According to Güthoff et al. [88], the following relations hold for the pre-factors B^{slow} and B^{fast},

$$B^{slow} = \frac{8\Gamma\left(\frac{3}{4}\right) \Omega M f^{slow} D_{\rm v}^{3/4} t^{1/4}}{\pi \sqrt{P^{slow}}} \tag{17}$$

and

$$B^{fast} = \frac{8\Gamma\left(\frac{3}{4}\right) \Omega M f^{fast} D_{\rm v}^{3/4} t^{1/4}}{\pi \sqrt{P^{fast}}} \tag{18}$$

Here M and Ω have the same meaning as in Eqs. (11)–(12), and Γ is the Euler gamma function.

---

[1] Note that special care was taken to pre-anneal the samples at a higher temperature of the subsequent diffusion annealing treatments to avoid GB motion.

[2] As it was mentioned, a strong, also non-linear solute segregation will shift the upper limit of the C-type kinetic regime to higher temperatures [82].

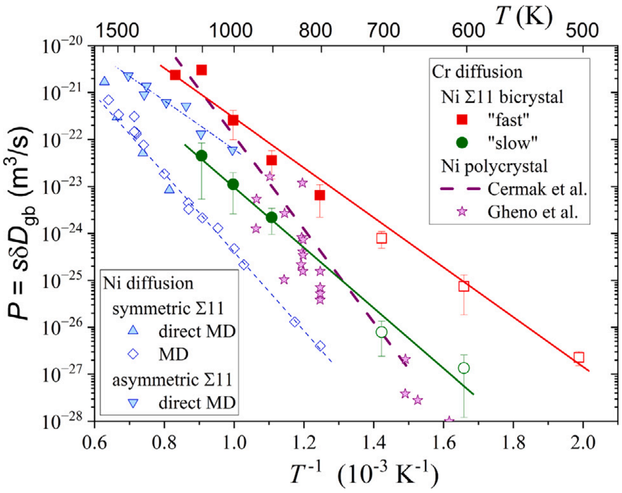

Fig. 5. Arrhenius diagram for grain boundary diffusion of Cr in the Ni $\Sigma 11$ bicrystal in the B- (filled squares and circles) and C-type (open squares and circles) kinetics regimes. The diffusion data are classified as relatively "slow" and "fast", circles and squares, respectively. The directly measured GB diffusion coefficients D_{gb} in the C-regime are multiplied by $\delta = 0.5$ nm and fitted together with the measured triple product values P in the B-regime. The Cr GB diffusion rates measured in polycrystalline Ni using the radiotracer method [24] (violet dashed line) and by SIMS [26] (violet stars) are shown for comparison. Moreover, the calculated Ni GB self-diffusion rates for the symmetric (triangles up and diamonds) and asymmetric (triangles down) facets are added. The results of both simulation methods (large-scale direct MD and the coefficients based on the MD study of single vacancy diffusion) are shown. (For interpretation of the references to color in this figure legend, the reader is referred to the web version of this article.)

Thus, the fraction of the "slow" segment can be determined from the relation which is similar to above Eq. (13),

$$\frac{f^{slow}}{1-f^{slow}} = \frac{B^{slow}}{B^{fast}}\left(\frac{P^{slow}}{P^{fast}}\right)^{1/2}, \tag{19}$$

and the results are summarized in Table 1. Note that the estimated fraction of the "fast" segments, varying between 1 to 3%, contradicts apparently the results of the macroscopic examination, Fig. 1, from which a ratio of about 70/30 for asymmetric/symmetric facets can be elucidated. This apparent contradiction will be resolved by the large-scale atomistic simulations, see below.

3.3.3. Transition BC regime

At 703 K, the diffusion experiment is found to be in the transition regime BC with the Le Claire parameter $\alpha \approx 0.5$ (see Table 1). According to the analysis by [82], the processing of such profiles as measured under the C-type conditions results in an acceptable uncertainty (the "correct" value is underestimated by 50% to 100%). If the profile is analyzed as measured under the B-type conditions, the uncertainties will be larger [82]. Therefore, we have processed the profile as measured under the C-type regime, Fig. 4(a). Two distinct contributions can be recognized again.

3.4. Temperature dependence of Cr GB diffusion

The measured GB diffusion rates are plotted in Fig. 5 in the Arrhenius coordinates.

Since the measured penetration profiles indicate the existence of two distinct contributions to the GB diffusion transport, a careful analysis of the corresponding temperature dependencies can provide valuable insights into the physical reasons for such a phenomenon. At the highest temperatures, $T \geq 1200$ K, only one contribution can reliably be recognized and contributions of two branches are clearly seen at 1103 K, 1003 K and 903 K, Fig. 5. The determined triple products P^{fast} corresponding to the deepest (shallow) branches of the penetration profiles follow a single Arrhenius line with the results at $T = 1203$ K, filled squares in Fig. 5. On the other hand, the P^{slow} values corresponding to the steeper branch reveal a different Arrhenius dependence, filled circles in Fig. 5.

The "slow" and "fast" branches, as revealed by the concentration profiles, are characterized by diffusion parameters which reasonably follow two distinct Arrhenius-type temperature dependencies, Fig. 5. This behavior strongly supports the view that the branches seen at different temperatures correspond systematically to the same microscopic features at all temperatures. Thus, we conclude that the given Ni grain boundary has different segments which are characterized by P^{fast} and P^{slow} GB diffusivities, and $P^{fast} \gg P^{slow}$ at the temperatures above 800 K.

At $T < 803$ K, the measurements were performed in the C-type kinetics regime (or in the transition BC regime at $T = 703$ K). The corresponding GB diffusion coefficients D_{gb}, multiplied by $\delta = 0.5$ nm, are plotted in Fig. 5 as open squares (D_{gb}^{fast}) or circles (D_{gb}^{slow}). The GB diffusivities represented by squares and circles in Fig. 5 are seen to follow common Arrhenius-type dependencies, though some minor deviations might be anticipated.

The fact that the P^{fast} and $\delta \cdot D_{gb}^{fast}$ or P^{slow} and $\delta \cdot D_{gb}^{slow}$ values follow their common (but different) Arrhenius lines allows several conclusions. First, the value $\delta = 0.5$ nm seems to be a reasonable estimate of the GB width for the Ni grain boundary for the studied temperature range, in line with previous findings [25,81]. Second, the Cr segregation factors s at Ni $\Sigma 11$ GB are about unity for both contributions or both segments of the interface.

Considering the entire datasets, the grain boundary triple products P for the "fast" and "slow" contributions to Cr diffusion along the given Ni GB are,

$$P^{fast} = 6.7^{+10}_{-4} \times 10^{-17} \exp\left(-\frac{103 \pm 6 \text{ kJ/mol}}{RT}\right) \text{ m}^3 \text{ s}^{-1} \tag{20}$$

and

$$P^{slow} = 1.9^{+5.8}_{-1.4} \times 10^{-17} \exp\left(-\frac{120 \pm 9 \text{ kJ/mol}}{RT}\right) \text{ m}^3 \text{ s}^{-1} \tag{21}$$

respectively.

Comparing the presently measured bicrystalline data with the triple products reported for the polycrystalline counterparts (5N purity) [24, 26] one can observe, that the Ni $\Sigma 11[110]$ GB presents a special case. In polycrystalline Ni, Čermák [24] found that Cr diffuses with a relatively high activation enthalpy of about $Q = 190$ kJ mol^{-1} in the temperature range between 858 K and 1208 K (see Fig. 5, violet dashed line). Gheno et al. [26] confirmed those results and extended the temperature range down to 623 K performing the measurements in the C-type kinetics as well (see Fig. 5, violet stars). Note that the D_{gb} values were measured by Gheno et al. in the C-type kinetics [26] and the double products $\delta \cdot D_{gb}$ are shown in Fig. 5 (with $\delta = 0.5$ nm).

The activation enthalpy of Cr diffusion in the Ni $\Sigma 11[110]$ GB for both branches is found to be smaller than in polycrystalline Ni and one can safely conclude that such interfaces were not present in the polycrystalline material used in the previous studies. However, the absolute D_{gb} values measured by Gheno et al. [26] show a large scatter and are generally not very different from the D_{gb} values measured for the slower facet type in the Ni $\Sigma 11$ bicrystal, Fig. 5.

Summarizing the experimental observations, we conclude that two distinct branches are resolved on the concentration profiles and the derived diffusivities follow two distinct Arrhenius-type temperature dependencies in the temperature interval examined. This behavior correlates qualitatively with the presence of two types of macroscopic facets distinguished for the $\Sigma 11[110]$ boundary, but not quantitatively. Is the symmetric or asymmetric facet corresponding to the "fast" diffusion contribution? Or should one look for another explanation? Is $s^{Cr} \approx 1$ a reliable approximation of the Cr segregation at the Ni $\Sigma 11(\bar{1}13)[110]$ GB? These issues will be addressed by atomistic simulations.

Table 2
Ab initio determined segregation energies of Cr at different positions of the Ni $\Sigma11(\bar{1}13)[110]$ and $\Sigma5(012)[100]$ GB compared to the literature data [76,97] (in eV/at).

Layer	$E_{seg}^{\Sigma11}$	$E_{seg}^{\Sigma5}$	$E_{seg}^{\Sigma5}$ [76]	$E_{seg}^{\Sigma5}$ Ref. [97]
0	−0.035	−0.058	−0.05	−0.06
1	0.006	−0.115		−0.12
2	−0.015	−0.060		−0.06
3	0.029	−0.020		−0.02

First, the ground state structure of the Ni $\Sigma11(\bar{1}13)[110]$ GB will be determined by an extended structure search using empirical potentials. Then, the thermal stability of the atomic structures with respect to potential GB phase transitions will be examined, since such transitions might affect the experimentally measured diffusion properties. The segregation tendency of Cr to the ground state GB structure will be determined by DFT calculations. Finally, large-scale MD simulations will provide an interpretation of the experimental findings.

3.5. Theoretical analysis of the equilibrium GB structure and GB segregation

3.5.1. Structure search with empirical potentials

To study the ground state atomic structure of the $\Sigma11(\bar{1}13)[110]$ GB in pure Ni, we performed a structure search using two EAM potentials [48,49] as described in the Methods section. The minimum energy structure at 0 K, Fig. 6(a) right, is composed of kites as highlighted in Fig. S1(c) in the Supplementary Materials. For the main EAM potential used in this work [48], we obtain a GB energy of 0.47 J/m^2 and an excess volume (the excess free volume per unit area) of 0.16 Å. The results of the analysis of GB excess values for the structure search are shown in Fig. S1(a)–(b) in the Supplementary Material. We could only find variations of the kite structure, separated into defective versions with vacancy-like and interstitial-like defects in the GB (snapshots in Supplemental Fig. S1(c)–(d)).

MD simulations of the GB annealed at 1400 K do not lead to any structural changes. Starting the annealing simulation with pre-inserted vacancies in the GB only leads to the same defective kite structures observed already in the 0 K structure search. However, even for the defect-free GB, a slight offset in z direction between the $(\bar{1}10)$ planes could be observed at higher temperatures, exemplified in Fig. 7.

A temperature sweep from 50 K to 1650 K with periodic boundary conditions shows that this offset does not exist at low temperatures but starts at around 1100 K for the main EAM potential used in this work [48]. For the earlier potential [49], which we only used as a comparison, the critical temperature was roughly 1500 K instead. The transition from zero offset to a finite offset is connected to very small energy differences and could either be interpreted as a change of microstate [96] or as a complexion transition. Proof of the latter would require thermodynamic analysis of discontinuities in the excess properties [56,57], which was not possible due to the noise in the data being greater than the (small) energy changes. We nevertheless mention this change, because it might affect the kinetic properties in the GB, see Sections 3.6 and 3.7.

3.5.2. Ab initio calculations

Using the atomistic structure of the $\Sigma11(\bar{1}13)[110]$ interface, ab initio calculations were performed and compared to calculations on the high energy $\Sigma5(012)[100]$ GB. The DFT-optimized structures are shown in Fig. 6(a). While the $\Sigma5$ GB exhibits relatively open structure units, the key features of the $\Sigma11$ GB are smaller units resulting in a more dense and bulk-like structure. This is also mirrored in the GB energies, Eq. (4), and the GB excess volume (in round brackets below), which were determined as 0.46 J/m^2 (0.12 Å) and 1.28 J/m^2 (0.32 Å) for the $\Sigma11$ GB and the $\Sigma5$ GB, respectively. Furthermore, these DFT calculations confirm the applicability of the EAM potential which predicted the $\Sigma11(\bar{1}13)[110]$ GB energy of 0.47 J/m^2.

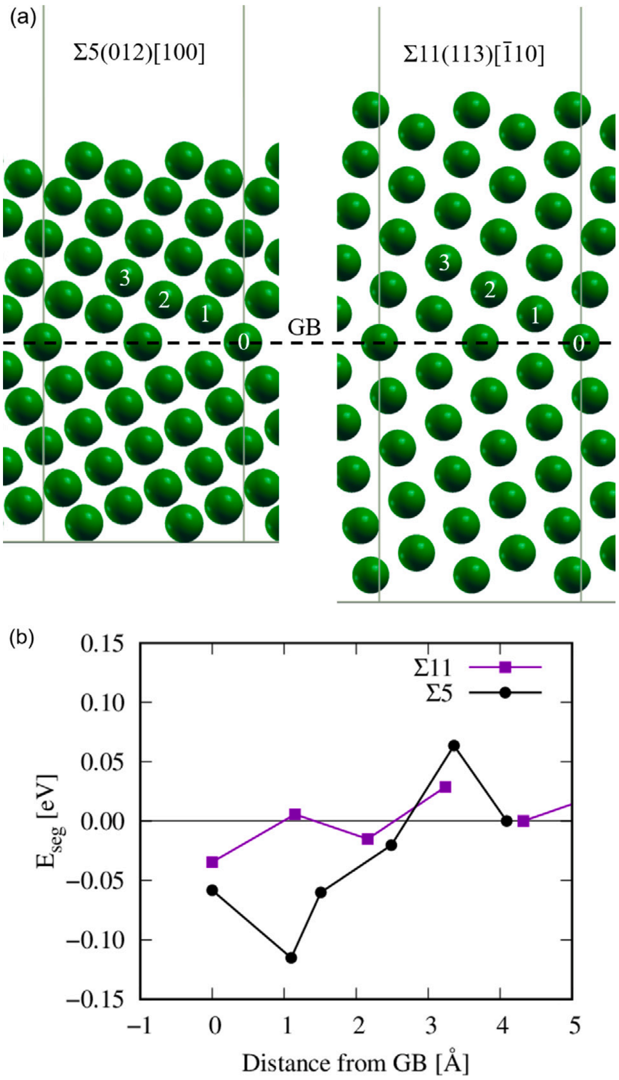

Fig. 6. Theoretical calculation using DFT of (**a**) CSL GBs $\Sigma5(012)[100]$ and $\Sigma11(\bar{1}13)[110]$ labeled with layer number. (**b**) Segregation energy as a function of solute location.

The segregation tendency of Cr to these Ni GBs was evaluated using Eq. (5). The resulting GB segregation profiles for both GBs are presented in Fig. 6(b). The segregation tendencies differ between the two GBs with the $\Sigma11$ GB exhibiting significantly lower segregation tendencies than the $\Sigma5$ GB. The strongest segregation energy for the $\Sigma11$ GB is −0.035 eV, whereas the $\Sigma5$ GB presents a maximum segregation energy of −0.115 eV, i.e. more than three times stronger. In addition, the $\Sigma11$ GB features only one type of segregation sites in contrast to three more for the $\Sigma5$ GB, making the latter a much more favorable interface for Cr segregation.

Thus, the DFT study predicts marginal, if any, segregation of Cr atoms to the Ni $\Sigma11$ GB with the symmetric GB plane, $s_{Cr} \approx 1$ reflecting its compact structure in contrast to a stronger segregation tendency for the $\Sigma5$ GB with its more open structure. This conclusion is in good agreement with the results and interpretation of the present radiotracer diffusion measurements, see Fig. 5.

Still, two major problems remain unresolved. First, which of the facets, the symmetrical or asymmetrical one corresponds to the “slow” (“fast”) GB branch? Second, the area fraction of the facets is about 70 to 30, respectively, while the “fast” branch corresponds to about 1% of the GB plane, according to the analysis of the radiotracer diffusion measurements, Table 1. We are going to address these questions with

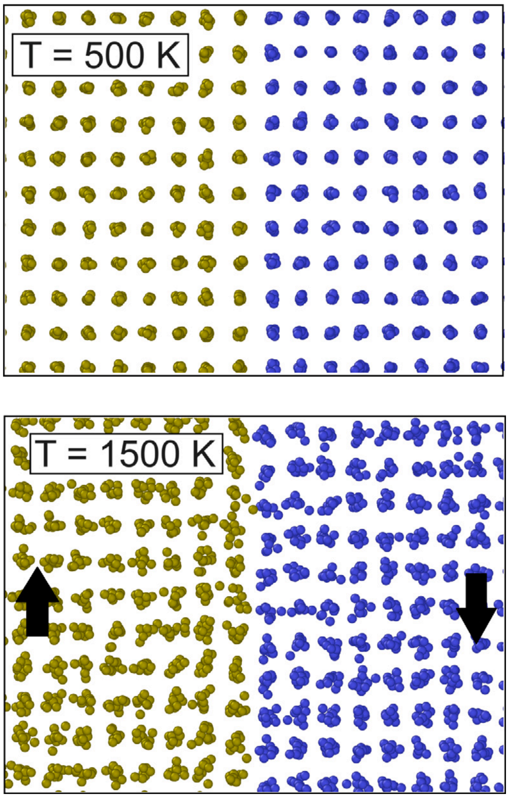

Fig. 7. Snapshots of the MD simulations illustrating the change of offset between $(\bar{1}10)$ planes during heating. Atoms of the different grains are shown in different colors (yellow and blue). The arrows at the higher temperature indicate the parallel shift of the grains along the tilt axis. (For interpretation of the references to color in this figure legend, the reader is referred to the web version of this article.)

Table 3
Calculated formation energy of point defects in bulk and inside $\Sigma 11(\bar{1}13)[110]$ GB.

energy	EAM	DFT [98]
E_v^{vac} (eV)	1.57	1.43
E_{gb}^{vac} (eV)	1.30	–
E_v^{sia} (eV)	3.95	4.07
E_{gb}^{sia} (eV)	2.23	–

the help of classical MD simulations, which enable to perform kinetic GB simulations with larger system sizes and at longer time scales than those used in DFT calculations.

3.6. Vacancy-mediated diffusion in the symmetric $\Sigma 11$ GB

We used finite-temperature MD simulation to reveal the basic mechanisms of GB diffusion. First, the symmetric tilt $\Sigma 11(\bar{1}13)[110]$ GB is studied. Table 3 shows the calculated formation energies of vacancies (E_v^{vac} and E_{gb}^{vac}) and self-interstitial atoms (E_v^{sia} and E_{gb}^{sia}) for the bulk crystal and the $\Sigma 11$ GB, respectively. For the bulk values, the predictions of the EAM potential agrees well with DFT calculations [98]. From the calculated energies it is clear that the GB diffusion is controlled by the migration of vacancies, since $E_{gb}^{vac} < E_{gb}^{sia}$, as in the bulk case.

The calculated diffusion coefficients of a single vacancy are shown in Fig. 8. Diffusion of vacancies inside GBs occurs much faster than in the bulk. Figs. 3 and 5 also show the calculated self-diffusion coefficients obtained from D^{vac} multiplied by the vacancy concentration. In general, the MD results are in good agreement with the experimental data on Cr diffusion.

Among other things, the MD simulation with the single vacancy revealed a slight change in the activation energy of diffusion along symmetric $\Sigma 11(\bar{1}13)[110]$ GB at $T \sim 1050$ K, which correlates with the existence of the specific structural transition described in Section 3.5.1 and illustrated in Fig. 7. This indicates that this parallel shift of the grains along the tilt axis may affect the kinetic properties of GB. In such a case, one might expect deviations from the otherwise linear Arrhenius-type temperature dependencies for both, "slow" and "fast" contributions. Since the experimental data, Fig. 5, do not reveal explicit kinks in the corresponding temperature dependencies (slight, but systematic deviations might be anticipated, though), we leave a closer analysis to future work.

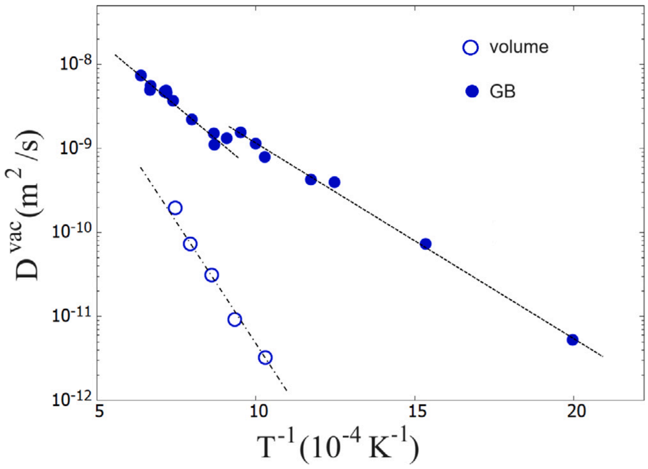

Fig. 8. The calculated temperature dependence of the vacancy diffusion coefficients in the bulk and inside the symmetric $\Sigma 11(\bar{1}13)[110]$ GB.

3.7. Large-scale MD simulation of GB diffusion

The computationally most expensive method in this work is the large-scale MD modeling. The basic idea of this method is that the concentration of vacancies in a large simulated crystal containing a surface should reach an equilibrium value after an annealing stage [67, 68]. We applied this method to study the self-diffusion for the symmetric and asymmetric, i.e. with a non-zero GB plane inclination, $\Sigma 11(\bar{1}13)[110]$ GBs. The modeling scheme and structure of the simulated asymmetrical facet are shown in Fig. 9.

As a most important result, after annealing, the asymmetric facet turned out to be transformed into a combination of regions with an ideal $\Sigma 11$ GB and a network of linear defects (i.e., disconnections), providing an average non-zero inclination of the GB plane. These disconnections are found to be channels for fast atomic diffusion along the GB plane, similar to ordinary dislocations in the crystalline bulk [99–101].

Fig. 10 displays a sequence of snapshots from the large-scale MD simulations. These snapshots clearly show that the diffusion mechanism depends on the character of the simulated facet. For the symmetric facet, the surface emits vacancies that control the diffusion process. However, for the asymmetric facet, the formation of point defects (vacancies and self-interstitial atoms) takes place inside the disconnections.

The linear density of the disconnections inside the simulated GB is probably 5–10 times higher than in the experiment. In fact, the distance between the simulated disconnections is comparable to the size of the disconnection core (see Fig. 9). Thus, the calculated diffusion coefficients are of the same order as the diffusion coefficients of the pipe diffusion along the disconnections. The directly calculated Ni self-diffusion coefficients for both facets are shown in Fig. 5. The calculated activation energies for the symmetric facet (1.77 eV) and the asymmetric facet (1.12 eV) agree well the measured values.

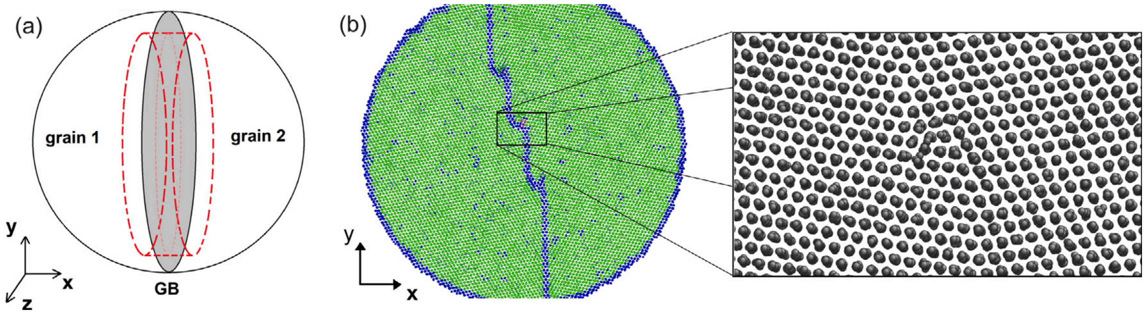

Fig. 9. Large-scale MD simulations of GB self-diffusion. (a) A scheme of the spherical particle used in the simulation. The GB plane is marked in grey, red dashed lines indicate the GB region where the self-diffusion coefficients were evaluated. (b) Slice of the simulated particle with the asymmetric facet. The color of the atoms corresponds to the results of the common neighbor analysis: green atoms indicate an fcc lattice, and blue atoms indicate defects (or a highly distorted structure). The inset shows the disconnection inside the GB. (For interpretation of the references to color in this figure legend, the reader is referred to the web version of this article.)

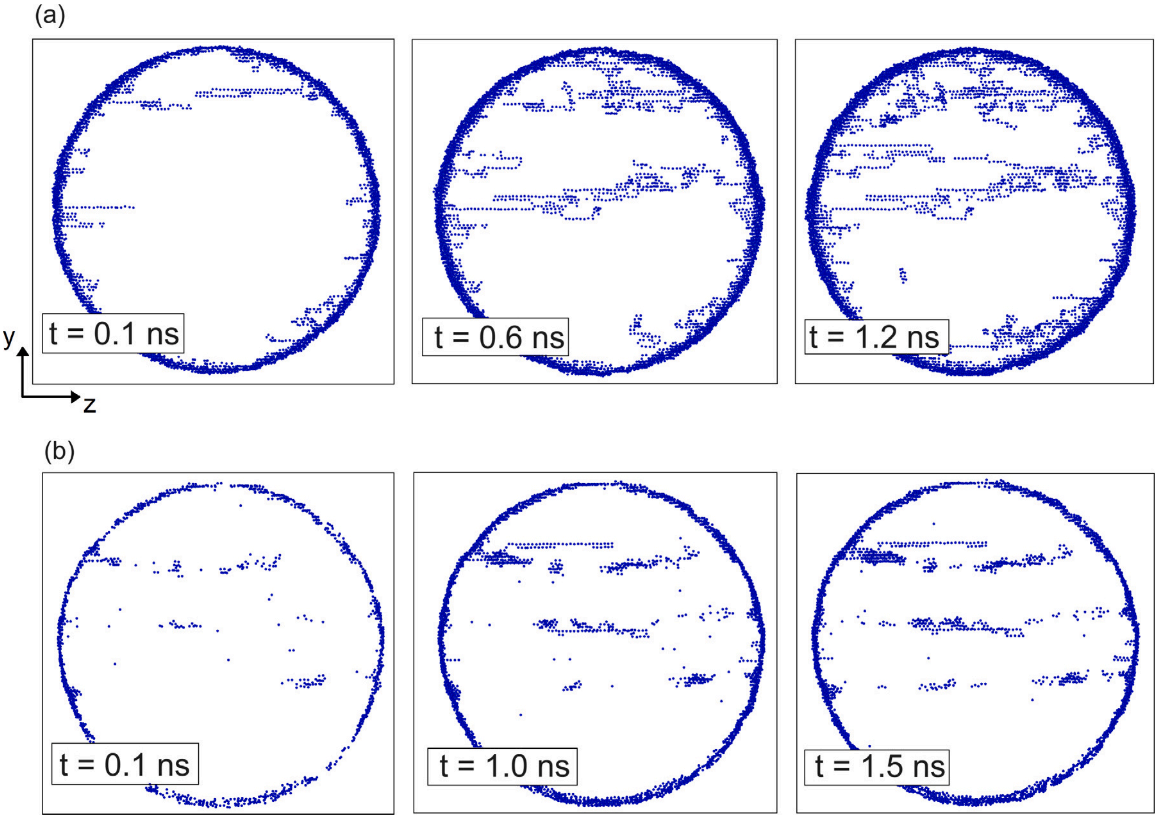

Fig. 10. Snapshots of the large-scale MD simulation. Only atoms with large displacements from the initial equilibrium positions (more than 1.3 Å) in the thin GB region are shown. This representation allows one to trace the migration of atoms. (a) The symmetric facet at $T = 1510$ K. (b) The asymmetric facet at $T = 1140$ K.

The ratio of the cross sections of the diffusion channels related to symmetric and asymmetric facets, A_{sym} and A_{asym} respectively, determines the relative diffusion fluxes along these short circuits, as they are seen in the experiment. For diffusion along the symmetric $\Sigma 11$ GB, $A_{sym} \sim \delta \cdot L_{sym}$, where L_{sym} is the length of the trace of the symmetric facet on the sample surface. Assuming that diffusion along the asymmetric facet is concentrated within the disconnections, their cross section, A_{asym}, is $A_{asym} \sim \delta^2 \cdot (\rho_l L_{asym})$ where ρ_l is a linear density of the disconnections on the GB plane (depending on the angle of inclination). Thus the ratio can be estimated as $A_{asym}/A_{sym} = \rho_l \delta \approx 0.01$ for the present experimental conditions.

Thus, the atomistic MD simulations confirm that the existence of the symmetric and asymmetric facets does explain the results of tracer diffusion measurements, even quantitatively. Since the Ni GB self-diffusion rates along the asymmetric facet significantly, by several orders of magnitude, exceed those along the symmetric facet, Fig. 5, it is safe to assume that the same relation holds for Cr GB diffusion as well. This conclusion is supported by very similar bulk diffusion rates of Ni and Cr in Ni, Fig. 3, and minor segregation of Cr atoms to the Ni $\Sigma 11$ GB (corroborated also within a model of GB diffusion in binary solid solutions [102,103]). Moreover, the activation energies of Cr diffusion along "fast" and "slow" branches are very similar to those for Ni self-diffusion along asymmetric and symmetric facets, Fig. 5. Even the relative fractions of the "fast" and "slow" paths, f^{fast}/f^{slow}, are similar to the ratio of the cross sections for asymmetric and symmetric facets. We conclude that the appearance of the disconnection-like defects within the asymmetric facets influences decisively the corresponding diffusion rates.

This behavior might be of a general nature and, probably, such an explanation might be applicable to the above-mentioned study of Rabkin et al. [92] on a Cu $\Sigma 3$ incoherent twin boundary.

3.8. Diffusion along an interface with line defects

So far, the diffusion rates of Cr atoms along the asymmetric facet with a network of disconnection-like defects was characterized by a single GB diffusion coefficient, $D_{\rm gb}^{fast}$. However, the atomistic simulations reveal significantly enhanced diffusion rates along the linear defects within such a boundary. Below we are proposing a model of the corresponding short-circuit diffusion that allows several estimates.

The analysis is based on the framework elaborated previously by one of the co-authors for the treatment of short-circuit diffusion in a complex microstructure with a hierarchy of the diffusion paths [85, 86,104] (these developments were also systematically elaborated in a recent textbook [82]). Accordingly, an asymmetric macro-facet is considered as composed of "ideal" nano-facets (let the size of these segments be d_0 and the corresponding diffusion coefficient $D_{\rm gb}^0$) delimited by a network of linear defects (which are characterized by the diffusion coefficients $D_{\rm gb}^d$ and the size of the defect cores δ_d). The linear GB defects are considered as disconnection-like ones and are distinguished by the index "^{d}". We assume that $D_{\rm v} \ll D_{\rm gb}^0 \ll D_{\rm gb}^d$.

For Cr atoms, we have to account for a potential segregation to these defects and the relevant segregation factor, $s_{\rm gb}^d$, is the ratio of the Cr concentration within the defects "cores", $c_{\rm gb}^d$, to that within the "ideal" nano-facets of the GBs, $c_{\rm gb}^0$, $s_{\rm gb}^d = c_{\rm gb}^d / c_{\rm gb}^0$.

The present experimental conditions correspond to the A-type kinetics of short-circuit diffusion within the asymmetric facets, since $\sqrt{D_{\rm gb}^0 t} \gg d_0$. Simultaneously, one has to account for the type B or type C diffusion along these interfaces with respect to the bulk diffusion. Thus, we are dealing either with B–A or C–A kinetics in a hierarchic microstructure according to the Divinski et al. classification [104]. In this paper, we will concentrate only on the diffusion transport along the given GB.

Then, the effective diffusion coefficient along the asymmetric facet, $D_{\rm gb}^{fast}$, is [10,82]

$$D_{\rm gb}^{fast} = \tau D_{\rm gb}^d + (1-\tau) D_{\rm gb}^0, \tag{22}$$

where $1-\tau$ and τ are the fractions of time spent by a diffusing atom within the "ideal" nano-facets and the disconnection-like defects, respectively, and

$$\tau \approx \frac{s_{\rm gb}^d \delta_d / d_0}{1 + s_{\rm gb}^d \delta_d / d_0}. \tag{23}$$

When $s_{\rm gb}^d \delta_d / d_0 \ll 1$, $D_{\rm gb}^{fast} \approx (s_{\rm gb}^d \delta_d / d_0) D_{\rm gb}^d + D_{\rm gb}^0$. Alternatively, if $s_{\rm gb}^d \delta_d / d_0 \gg 1$, $D_{\rm gb}^{fast} \approx D_{\rm gb}^d$, since $\tau \approx 1$.

Since the DFT calculations of Cr segregation tendencies at asymmetric facets would be highly demanding, we employed atomistic simulations using the ADP potential of Howells and Mishin [50]. First, we evaluated the performance of the ADP potential for predicting the Cr segregation energies for the symmetric $\Sigma5(012)[100]$ and $\Sigma11(\bar{1}13)[110]$ GBs, by comparing the results with the current DFT data, Fig. 6. The Cr segregation energies at the positions 2 and 3 of the $\Sigma11(\bar{1}13)[110]$ GB are negligible (less than −0.01 eV/at) in full agreement with the DFT data, but a moderate segregation is predicted for the sites 1 and 0, about −0.095 and −0.106 eV/at, respectively. For the $\Sigma5(012)[100]$ GB, the calculated segregation energies are largest at the site 2 in Fig. 6(a), left panel, and equal to −0.278 eV/at. However, no segregation is predicted for the site 1 using the ADP potential, though this site is most attractive according to the DFT calculations, Table 2. We conclude that the ADP potential potentially overestimates the total segregation tendency of Cr to Ni GBs (note that the multi-site segregation model has to be used in this case [105–107]) and the corresponding results have to be treated with caution.

We evaluated the segregation energies for different sites of the asymmetric facet shown in Fig. 9. At 0 K, the segregation energies are less than 0.04 eV/at for all positions belonging to the "ideal" nano-facets (thus fully in line with the DFT results for the symmetric facets of the $\Sigma11$ GB), but some positions within the disconnection-like cores reveal the segregation energies of about −0.2 eV/at (with respect to the positions within the crystalline bulk).

The effective segregation factor, $s_{\rm gb}^{fast}$, for the asymmetric facet can be written as $s_{\rm gb}^{fast} = [1 + \delta_d / d_0 (s_{\rm gb}^d - 1)] s_{\rm gb}^0$, where $s_{\rm gb}^0 \approx 1$ is the segregation factor for the "ideal" nano-facets, i.e. the ratio of Cr concentration within those facets to that within the crystalline bulk.

Now, some estimates can be drawn using the results of the atomistic simulation, Fig. 9(b), using $\delta_d = 0.5$ nm and $d_0 = 5$ nm. The effective segregation factor for the asymmetric facet is nearly unity at $T > 700$ K and it may increase to 5 or even 10 at 600 or 500 K. However, since these values are probably overestimated, a general correctness of the analysis of the experimental data assuming small values of s for the asymmetric facet, too, is confirmed.

The value of τ is about unity at $T < 700$ K, suggesting that the measured Cr diffusion coefficients $D_{\rm gb}^{fast}$ correspond indeed to the diffusion rates within the disconnection-like cores, $D_{\rm gb}^d$. Assuming that the diffusion rates along the symmetric facet, $D_{\rm gb}^{slow}$, and those for the "ideal" segments of the asymmetric facet, $D_{\rm gb}^0$, are similar, we conclude that the disconnection-like defects reveal faster rates of the diffusion transport by one to two orders of magnitude with respect to the "defect-free" compact interfaces.

At higher temperatures, the value of τ decreases to about 0.4 at $T =$ 1200 K. However, the ratio $P^{fast}/P^{slow} \approx \left(s_{\rm gb}^{fast}/s_{\rm gb}^{slow}\right)\left(D_{\rm gb}^{fast}/D_{\rm gb}^{slow}\right) \approx \left(D_{\rm gb}^{fast}/D_{\rm gb}^{slow}\right)$ still corresponds roughly to the diffusion enhancement within the disconnection-like defects of the asymmetric facets.

4. Summary and conclusions

Grain boundary diffusion of Cr is measured in a Ni $\Sigma11[110]$ bicrystal applying the radiotracer technique. The measurements are performed in an extended temperature interval in both B- and C-types of kinetic regimes.

Although tracer diffusion is measured along a (nominally) single interface in a bicrystalline material, two diffusion branches are systematically resolved, a relatively "slow" and a relatively "fast" one. These experimental findings correlate with the presence of distinct (macroscopic) facets of the boundary, which were identified as symmetric facets and asymmetrical ones.

The analysis of the tracer diffusion data suggests that Cr marginally segregates to the Ni GB, $s_{\rm Cr} \approx 1$, and the diffusional GB width δ is about 0.5 nm. These evaluations hold true for both diffusion contributions.

The interpretation of the segregation factor from the tracer diffusion data as $s_{\rm Cr} \approx 1$ is fully supported by DFT calculations for the symmetric facet of the Ni $\Sigma11(\bar{1}13)[110]$ GB. This result is related to its compact structure with atomic coordination close to bulk fcc, whereas it is demonstrated that a more open interface structure, like the $\Sigma5$ GB, would result in a significantly stronger segregation tendency.

Atomistic simulations of Ni GB self-diffusion are employed to provide insights into possible reasons behind the observed separation of the tracer diffusion results into "fast" and "slow" branches, predicting that the area fraction of the "fast" diffusion branch is only a fraction of a percentage of that of the "slow" branch, whereas about a 30/70 ratio was found between the areas of the symmetric and asymmetric facets.

First, the atomistic simulations evidence directly that the "fast" ("slow") GB diffusion branch corresponds to the asymmetric (symmetric) facet of the Ni $\Sigma11$ GB. The asymmetric facet is found to contain a network of GB defects (disconnections) which decisively contribute to the enhanced diffusion transport. Furthermore, this diffusion transport is largely confined within the corresponding GB dislocation (or disconnection) cores, which ultimately resolves the apparent contradiction between the fraction of the macroscopic facets and the relative fraction of the "fast" diffusion branch.

Thus, the diffusion enhancement along the disconnection-like defects with respect to the "defect-free" GBs is estimated for the first time and it is shown to approach several orders of magnitude at low temperatures.

Second, the GB structure is found to evolve continuously with increasing temperature revealing features of a continuous GB transition. These findings from the atomistic simulations correlate with a minor, but systematic deviation of the Cr GB diffusion coefficients from the anticipated linear Arrhenius-type temperature dependence.

Finally, the present study highlights the importance of the GB disconnection (dislocation) network, for a reliable prediction and description of the kinetic and thermodynamic properties of GBs. The presence of these defects can substantially change and even determine the diffusion rates of elements along GBs.

CRediT authorship contribution statement

Shraddha V. Sevlikar: Writing – original draft, Investigation, Data curation. **G. Mohan Muralikrishna:** Writing – original draft, Investigation, Data curation. **Daniel Gaertner:** Investigation. **Sergei Starikov:** Writing – review & editing, Software, Investigation, Data curation. **Tobias Brink:** Writing – review & editing, Software, Investigation, Data curation. **Daniel Scheiber:** Writing – review & editing, Investigation, Formal analysis, Data curation, Conceptualization. **Daria Smirnova:** Writing – review & editing, Investigation, Formal analysis, Data curation. **Daniel Irmer:** Investigation. **Bengü Tas:** Investigation. **Vladimir A. Esin:** Writing – review & editing, Investigation, Data curation. **Vsevolod I. Razumovskiy:** Writing – review & editing, Supervision, Formal analysis, Data curation. **Christian H. Liebscher:** Writing – review & editing, Investigation, Data curation. **Gerhard Wilde:** Writing – review & editing, Resources, Funding acquisition. **Sergiy V. Divinski:** Writing – review & editing, Supervision, Project administration, Funding acquisition, Formal analysis, Conceptualization.

Declaration of competing interest

The authors declare that they have no known competing financial interests or personal relationships that could have appeared to influence the work reported in this paper.

Acknowledgments

The research was funded by the French-German ANR-DFG DIPLOX project (DI 1418/16-1 and ANR-17-CE08-0049). A partial support from DFG, Germany via research grants DI 1418/19-1, WI 1899/44-1 and LI 2133/7-1 is acknowledged. T.B. acknowledges funding from the European Research Council (ERC) under the European Union's Horizon 2020 research and innovation program (Grant agreement No. 787446; GB-CORRELATE). G.M.M is grateful to the Alexander-von-Humboldt Foundation for awarding a fellowship to pursue research at the University of Muenster, Germany. V.I.R and D.S. acknowledge the financial support from the Austrian ministry for traffic, innovation and technology, BMVIT and voestalpine BÖHLER Edelstahl GmbH & Co KG within the framework of the PREHY project (FFG number 891181).

Appendix A. Supplementary data

Supplementary material related to this article can be found online at https://doi.org/10.1016/j.actamat.2024.120229.

References

[1] A. Gloria, R. Montanari, M. Richetta, A. Varone, Alloys for aeronautic applications: State of the art and perspectives, Metals 9 (2019) 662.

[2] R. Celin, F. Tehovnik, Degradation of a Ni-Cr-Fe alloy in a pressurised-water nuclear power plant, Mater. Technol. 45 (2011) 151.

[3] Z. Zhu, J. Chen, Y. Cai, J. Li, Y. Shen, Effect of heat treatment on the microstructure and fracture behaviors of a Ni–Cr–Fe superalloy, Adv. Eng. Mater. 22 (2020) 1901070.

[4] G. Smola, R. Gawel, K. Kyziol, M. Miszczak, Z. Grzesik, Influence of nickel on the oxidation resistance at high temperatures of thin chromium coatings, Oxid. Met. 91 (2019) 625.

[5] E. Kashkarov, D. Sidelev, M. Syrtanov, C. Tang, M. Steinbrück, Oxidation kinetics of cr-coated zirconium alloy: Effect of coating thickness and microstructure, Corros. Sci. 175 (2020) 108883.

[6] A. Michau, F. Maury, F. Schuster, F. Lomello, J.-C. Brachet, E. Rouesne, M. Le Saux, R. Boichot, M. Pons, High-temperature oxidation resistance of chromium-based coatings deposited by DLI-MOCVD for enhanced protection of the inner surface of long tubes, Surf. Coat. Technol. 349 (2018) 1048.

[7] W. Kuang, M. Song, G.S. Was, Insights into the stress corrosion cracking of solution annealed alloy 690 in simulated pressurized water reactor primary water under dynamic straining, Acta Mater. 151 (2018) 321.

[8] T. Moss, G.S. Was, Accelerated stress corrosion crack initiation of alloys 600 and 690 in hydrogenated supercritical water, Metall. Mater. Trans. A 48 (2017) 1613.

[9] L. Priester, Grain Boundaries: From Theory to Engineering, vol. 172, Springer Science & Business Media, 2012.

[10] I. Kaur, Y. Mishin, W. Gust, Fundamentals of Grain and Interface Boundary Diffusion, Wiley & Sons LTD, 1995.

[11] N.E. Dowling, S.L. Kampe, M.V. Kral, Mechanical Behavior of Materials: Engineering Methods for Deformation, Fracture, and Fatigue, Pearson, 2012.

[12] Y. Mishin, C. Herzig, J. Bernardini, W. Gust, Grain boundary diffusion: fundamentals to recent developments, Int. Mater. Rev. 42 (1997) 155.

[13] M.B. Ponnuchamy, G.M. Muralikrishna, V.R. Mannava, G.S. Reddy, Preparation of nanocrystalline nickel oxide from nickel hydroxide using spark plasma sintering and inverse Hall-Petch related densification, Ceram. Int. 44 (2018) 15019.

[14] T. Watanabe, Grain boundary engineering: historical perspective and future prospects, J. Mater. Sci. 46 (2011) 4095.

[15] E. Rabkin, W. Gust, Grain boundary diffusion and segregation in the solid state phase transformations, MRS Online Proc. Libr. 527 (1998) 255.

[16] L.S. Shvindlerman, B.B. Straumal, Grain boundary diffusion and grain boundary phase transformations, in: Diffusion in Metals and Alloys, DIMETA 88, in: Defect and Diffusion Forum, vol. 66, Trans Tech Publications Ltd, 1990, pp. 649–666.

[17] P.E. L'vov, R.T. Sibatov, Phase-field model of grain boundary diffusion in nanocrystalline solids: Anisotropic fluctuations, anomalous diffusion, and precipitation, J. Appl. Phys. 132 (2022) 124304.

[18] S.V. Divinski, H. Edelhoff, S. Prokofjev, Diffusion and segregation of silver in copper $\Sigma 5(310)$ grain boundary, Phys. Rev. B 85 (2012) 144104.

[19] T. Frolov, S.V. Divinski, M. Asta, Y. Mishin, Effect of interface phase transformations on diffusion and segregation in high-angle grain boundaries, Phys. Rev. Lett. 110 (2013) 255502.

[20] T. Frolov, D. Olmsted, M. Asta, Y. Mishin, Structural phase transformations in metallic grain boundaries, Nature Commun. 4 (2013) 1899.

[21] P.R. Cantwell, T. Frolov, T.J. Rupert, A.R. Krause, C.J. Marvel, G.S. Rohrer, J.M. Rickman, M.P. Harmer, Grain boundary complexion transitions, Annu. Rev. Mater. Res. 50 (2020) 465.

[22] T. Meiners, T. Frolov, R. Rudd, G. Dehm, C. Liebscher, Observations of grain-boundary phase transformations in an elemental metal, Nature 579 (2020) 375.

[23] L. Langenohl, T. Brink, R. Freitas, T. Frolov, G. Dehm, C. Liebscher, Dual phase patterning during a congruent grain boundary phase transition in elemental copper, Nature Commun. 13 (2022) 3331.

[24] J. Čermák, Grain boundary self-diffusion of ^{51}Cr and ^{59}Fe in austenitic Ni-Fe-Cr alloys, Mater. Sci. Eng. 279 (1991) A148.

[25] S.V. Divinski, G. Reglitz, G. Wilde, Grain boundary self-diffusion in polycrystalline nickel of different purity levels, Acta Mater. 58 (2010) 386.

[26] T. Gheno, F. Jomard, C. Desgranges, L. Martinelli, Grain boundary diffusion of chromium in polycrystalline nickel studied by SIMS, Materialia 6 (2019) 100283.

[27] A.N. Aleshin, V.Y. Aristov, B.S. Bokshtein, L.S. Shvindlerman, Kinetic properties of $< 111 >$ tilt boundaries in aluminium, Phys. Status Solidi 45 (1978) 359.

[28] T. Surholt, D. Molodov, C. Herzig, Orientation dependence of Ge diffusion along symmetrical [111] tilt grain boundaries in Al, Acta Mater. 46 (1998) 5345.

[29] P. Klugkist, A. Aleshin, W. Lojkowski, L. Shvindlerman, W. Gust, E. Mittemeijer, Diffusion of Zn along tilt grain boundaries in Al: pressure and orientation dependence, Acta Mater. 49 (2001) 2941.

[30] A. Aleshin, R. Faulkner, D. Molodov, L. Shvindlerman, Compensation effect for grain boundary diffusion in a bicrystalline experiment, Interface Sci. 10 (2002) 5.

[31] A. Aleshin, Relations between the parameters of grain-boundary diffusion of zinc in aluminum, Russ. Metall. 2006 (2006) 150.

[32] W. Lojkowski, U. Södervall, S. Mayer, W. Gust, The effect of pressure on indium diffusion along $< 001 >$ tilt grain boundaries in copper bicrystals, Interface Sci. 6 (1998) 187.

[33] E. Budke, T. Surholt, S. Prokofjev, L. Shvindlerman, C. Herzig, Tracer diffusion of Au and Cu in a series of near $\Sigma = 5(310)[001]$ symmetrical Cu tilt grain boundaries, Acta Mater. 47 (1999) 385.

[34] S. Schwarz, B. Kempshall, L. Giannuzzi, F. Stevie, Utilizing the SIMS technique in the study of grain boundary diffusion along twist grain boundaries in the Cu(Ni) system, Acta Mater. 50 (2002) 5079.

[35] S.V. Divinski, B.S. Bokstein, Recent advances and unsolved problems of grain boundary diffusion, Defect Diffus. Forum 1 (2011) 309–310.

[36] J. Sommer, C. Herzig, S. Mayer, W. Gust, Grain boundary self-diffusion in silver bicrystals, in: Diffusion in Metals and Alloys, DIMETA 88, in: Defect and Diffusion Forum, vol. 66, Trans Tech Publications Ltd, 1990, pp. 843–848.

[37] J. Sommer, C. Herzig, T. Muschik, W. Gust, Temperature dependence and anisotropy of grain boundary self-diffusion along $\Sigma = 5 < 001 >$ tilt boundaries in Ag, Acta Metall. Mater. 43 (1995) 1099.

[38] R.F. Canon, J.P. Stark, Grain boundary self-diffusion in nickel, J. Appl. Phys. 40 (1969) 4366.

[39] H. Edelhoff, S.I. Prokofjev, S.V. Divinski, The C-regime measurements of grain boundary diffusion of silver in copper $\Sigma5$ (310) bicrystal, Scr. Mater. 64 (2011) 374.

[40] D. Gaertner, L. Belkacemi, V. Esin, F. Jomard, A. Fedotov, J. Schell, Y. Osinskaya, A. Pokoev, C. Duhamel, A. Paul, S. Divinski, Techniques of tracer diffusion measurements in metals, Alloys Compd. Diffus. Found. 29 (2021) 31.

[41] G. Bordiert, W. Scheck, K. Wieder, Precision measurement of the γ-ray energies from the radioactive decay of ^{51}Cr, ^{169}Yb, ^{170}Tm, ^{192}Ir and ^{203}Hg, Z. Nat.forsch. A 30 (1975) 274.

[42] H.O.K. Monma, H. Suto, Diffusion of ^{63}Ni and ^{51}Cr in nickel-chromium alloys, J. Jpn. I. Met 28 (1964) 188.

[43] J. Růžičková, B. Million, Self-diffusion of the components in the F.C.C. phase of binary solid solutions of the Fe–Ni–Cr system, Mater. Sci. Eng. 50 (1981) 59.

[44] S. Jung, T. Yamane, Y. Minamino, K. Hirao, H. Araki, S. Saji, Interdiffusion and its size effect in nickel solid solutions of Ni-Co, Ni-Cr and Ni-Ti systems, J. Mater. Sci. Lett. 11 (1992) 1333–1337.

[45] T. Gheno, F. Jomard, C. Desgranges, L. Martinelli, Tracer diffusion of Cr in Ni and Ni-22Cr studied by SIMS, Materialia 3 (2018) 145.

[46] S. Plimpton, Fast parallel algorithms for short-range molecular dynamics, J. Comput. Phys. 117 (1995) 1.

[47] A.P. Thompson, H.M. Aktulga, R. Berger, D.S. Bolintineanu, W.M. Brown, P.S. Crozier, P.J. in 't Veld, A. Kohlmeyer, S.G. Moore, T.D. Nguyen, R. Shan, M.J. Stevens, J. Tranchida, C. Trott, S.J. Plimpton, LAMMPS - a flexible simulation tool for particle-based materials modeling at the atomic, meso, and continuum scales, Comput. Phys. Comm. 271 (2022) 108171, https://lammps.org/.

[48] Y. Mishin, Atomistic modeling of the γ and γ'-phases of the Ni–Al system, Acta Mater. 52 (2004) 1451.

[49] Y. Mishin, D. Farkas, M.J. Mehl, D.A. Papaconstantopoulos, Interatomic potentials for monoatomic metals from experimental data and ab initio calculations, Phys. Rev. B 59 (1999) 3393.

[50] C.A. Howells, Y. Mishin, Angular-dependent interatomic potential for the binary Ni–Cr system, Modelling Simul. Mater. Sci. Eng. 26 (2018) 085008.

[51] E.W. Hart, Two-dimensional phase transformation in grain boundaries, Scr. Metall. 2 (1968) 179.

[52] J. W. Cahn, Transitions and phase equilibria among grain boundary structures, J. Phys. Colloques 43 (1982) C6.

[53] C. Rottman, Theory of phase transitions at internal interfaces, J. Phys. Colloques 49 (1988) C5.

[54] M. Tang, W.C. Carter, R.M. Cannon, Diffuse interface model for structural transitions of grain boundaries, Phys. Rev. B 73 (2006) 024102.

[55] S.J. Dillon, M. Tang, W.C. Carter, M.P. Harmer, Complexion: A new concept for kinetic engineering in materials science, Acta Mater. 55 (2007) 6208.

[56] T. Frolov, Y. Mishin, Phases, phase equilibria, and phase rules in low-dimensional systems, J. Chem. Phys. 143 (2015) 044706.

[57] T. Brink, L. Langenohl, H. Bishara, G. Dehm, Universality of grain boundary phases in fcc metals: Case study on high-angle [111] symmetric tilt grain boundaries, Phys. Rev. B 107 (2023) 054103.

[58] T. Frolov, M. Asta, Y. Mishin, Segregation-induced phase transformations in grain boundaries, Phys. Rev. B 92 (2015) 020103.

[59] N.J. Peter, T. Frolov, M.J. Duarte, R. Hadian, C. Ophus, C. Kirchlechner, C.H. Liebscher, G. Dehm, Segregation-induced nanofaceting transition at an asymmetric tilt grain boundary in copper, Phys. Rev. Lett. 121 (2018) 255502.

[60] N. Zhou, C. Hu, J. Luo, Grain boundary segregation transitions and critical phenomena in binary regular solutions: A systematics of complexion diagrams with universal characters, Acta Mater. 221 (2021) 117375.

[61] D. K. R., A model for grain boundary thermodynamics, RSC Adv. 10 (2020) 26728.

[62] G. Gottstein, L.S. Shvindlerman, Grain Boundary Migration in Metals Thermodynamics, Kinetics, Applications, second ed., CRS Press, 2010.

[63] A. Sutton, R. Balluffi, Interfaces in Crystalline Materials, Clarendon Press, Oxford, UK, 1995.

[64] Q. Zhu, A. Samanta, B. Li, R.E. Rudd, T. Frolov, Predicting phase behavior of grain boundaries with evolutionary search and machine learning, Nature Commun. 9 (2018) 467.

[65] A. Metsue, A. Oudriss, J. Bouhattate, X. Feaugas, Contribution of the entropy on the thermodynamic equilibrium of vacancies in nickel, J. Chem. Phys. 140 (2014) 104705.

[66] Y. Gong, B. Grabowski, A. Glensk, F. Körmann, J. Neugebauer, R.C. Reed, Temperature dependence of the Gibbs energy of vacancy formation of fcc Ni, Phys. Rev. B 97 (2018) 214106.

[67] S. Starikov, M. Mrovec, R. Drautz, Study of grain boundary self-diffusion in iron with different atomistic models, Acta Mater. 188 (2020) 560.

[68] S. Starikov, A. Abbass, R. Drautz, M. Mrovec, Disordering complexion transition of grain boundaries in bcc metals: Insights from atomistic simulations, Acta Mater. 261 (2023) 119399.

[69] G. Kresse, J. Hafner, *Ab initio* molecular dynamics for liquid metals, Phys. Rev. B 47 (1993) 558.

[70] G. Kresse, J. Furthmüller, Efficiency of ab-initio total energy calculations for metals and semiconductors using a plane-wave basis set, Comput. Mater. Sci. 6 (1996) 15.

[71] G. Kresse, J. Furthmüller, Efficient iterative schemes for *ab initio* total-energy calculations using a plane-wave basis set, Phys. Rev. B 54 (1996) 11169.

[72] G. Kresse, D. Joubert, From ultrasoft pseudopotentials to the projector augmented-wave method, Phys. Rev. B 59 (1999) 1758.

[73] P.E. Blöchl, Projector augmented-wave method, Phys. Rev. B 50 (1994) 17953.

[74] J.P. Perdew, K. Burke, M. Ernzerhof, Generalized gradient approximation made simple, Phys. Rev. Lett. 77 (1996) 3865.

[75] P. Haas, F. Tran, P. Blaha, Calculation of the lattice constant of solids with semilocal functionals, Phys. Rev. B 79 (2009) 085104.

[76] V. Razumovskiy, A. Lozovoi, I. Razumovskii, First-principles-aided design of a new Ni-base superalloy: Influence of transition metal alloying elements on grain boundary and bulk cohesion, Acta Mater. 82 (2015) 369.

[77] C. Minkwitz, C. Herzig, E. Rabkin, W. Gust, The inclination dependence of gold tracer diffusion along a $\Sigma3$ twin grain boundary in copper, Acta Mater. 47 (1999) 1231.

[78] K. Maier, H. Mehrer, E. Lessmann, W. Schüle, Self-diffusion in nickel at low temperatures, Phys. Status Solidi 78 (1976) 689.

[79] A. Glensk, B. Grabowski, T. Hickel, J. Neugebauer, Breakdown of the arrhenius law in describing vacancy formation energies: The importance of local anharmonicity revealed by ab initio thermodynamics, Phys. Rev. X 4 (2014) 011018.

[80] L. Harrison, Influence of dislocations on diffusion kinetics in solids with particular reference to the alkali halides, Trans. Faraday Soc. 57 (1961) 1191.

[81] D. Prokoshkina, V. Esin, G. Wilde, S. Divinski, Grain boundary width, energy and self-diffusion in nickel: Effect of material purity, Acta Mater. 61 (2013) 5188.

[82] A. Paul, T. Laurila, V. Vuorinen, S. Divinski, Thermodynamics, Diffusion and the Kirkendall Effect in Solids, Springer, 2014.

[83] I. Belova, T. Fiedler, N. Kulkarni, G. Murch, The harrison diffusion kinetics regimes in solute grain boundary diffusion, Phil. Mag. 92 (2012) 1748.

[84] D.L. Beke, I. Gödény, G. Erdélyi, F.J. Kedves, The temperature dependence of grain-boundary diffusion of ^{65}Zn in polycrystalline aluminium, Phil. Mag. A 56 (1987) 659.

[85] S.V. Divinski, F. Hisker, Y.-S. Kang, J.-S. Lee, C. Herzig,^{59}Fe grain boundary diffusion in nanostructured γ-Fe–Ni. Part I: Radiotracer experiments and Monte-Carlo simulation in the type-A and B kinetic regimes, Int. J. Mater. Res. 93 (2002) 256.

[86] S. Divinski, F. Hisker, Y.-S. Kang, J.-S. Lee, C. Herzig,^{59}Fe grain boundary diffusion in nanostructured γ-Fe–Ni. Part II: Effect of bimodal microstructure on diffusion behavior in type-C kinetic regime, Int. J. Mater. Res. 93 (2002) 265.

[87] A. Glaeser, J. Evans, Effect of grain boundary migration on apparent boundary diffusion coefficients, Acta Metall. 34 (1986) 1545.

[88] F. Güthoff, Y. Mishin, C. Herzig, Self-diffusion along stationary and moving grain boundaries in α-Hf, Int. J. Mater. Res. 84 (1993) 584.

[89] S. Divinski, M. Lohmann, T. Surholt, C. Herzig, Grain boundary motion during Ag and Cu grain boundary diffusion in Cu polycrystals, Interface Sci. 9 (2001) 357.

[90] B.S. Bokstein, V.E. Fradkov, D.L. Beke, Grain boundary segregation and grain-boundary heterodiffusion, Phil. Mag. A 65 (1992) 277.

[91] S.V. Divinski, M. Lohmann, S.I. Prokofjev, C. Herzig, Quantitative experiments on the transition between linear to non-linear segregation of Ag in Cu bicrystals studied by radiotracer grain boundary diffusion, Int. J. Mater. Res. 96 (2005) 1181.

[92] E. Rabkin, C. Minkwitz, C. Herzig, L. Klinger, Evidence for structural multiplicity of the $\Sigma = 3$ incoherent twin boundary in Cu from grain-boundary diffusion measurements, Phil. Mag. Lett. 79 (1999) 409.

[93] A. Le Claire, The analysis of grain boundary diffusion measurements, Br. J. Appl. Phys. 14 (1963) 351.

[94] T. Suzuoka, Exact solutions of two ideal cases in grain boundary diffusion problem and the application to sectioning method, J. Phys. Soc. Japan 19 (1964) 839.

[95] H. Levine, C. MacCallum, Grain boundary and lattice diffusion in polycrystalline bodies, J. Appl. Phys. 31 (1960) 595.

[96] S. Ahmad, T. Brink, C.H. Liebscher, G. Dehm, Microstates and defects of incoherent $\Sigma 3$ [111] twin boundaries in aluminum, Acta Mater. 243 (2023) 118499.

[97] S. He, W. Ecker, O.E. Peil, R. Pippan, V.I. Razumovskiy, The effect of solute atoms on the bulk and grain boundary cohesion in Ni: Implications for hydrogen embrittlement, Materialia 21 (2022) 101293.

[98] J. Tucker, T. Allen, D. Morgan, Ab initio defect properties for modeling radiation-induced segregation in Fe-Ni-Cr alloys, in: Proc. Int. Symp. Environ. Degradat. Mater. Nucl. Power Syst. 13th, Vol. 23, Whistler, BC, Can. Apr. 19, Citeseer, 2007, pp. 1004–1014.

[99] G.P. Pun, Y. Mishin, A molecular dynamics study of self-diffusion in the cores of screw and edge dislocations in aluminum, Acta Mater. 57 (2009) 5531.

[100] S. Starikov, V. Jamebozorgi, D. Smirnova, R. Drautz, M. Mrovec, Atomistic simulations of pipe diffusion in bcc transition metals, Acta Mater. 260 (2023) 119294.

[101] I. Chesser, R.K. Koju, Y. Mishin, Atomic-level mechanisms of short-circuit diffusion in materials, Int. J. Mater. Res. 115 (2024) 85.

[102] V.A. Esin, B.S. Bokstein, Effect of atomic interaction on grain boundary diffusion in the B regime, Acta Mater. 60 (2012) 5109.

[103] V.A. Esin, Y. Souhar, Solvent grain boundary diffusion in binary solid solutions: a new approach to evaluate solute grain boundary segregation, Phil. Mag. 94 (2014) 4066.

[104] S. Divinski, F. Hisker, Y.-S. Kang, J.-S. Lee, C. Herzig, Ag diffusion and interface segregation in nanocrystalline γ-FeNi alloy with a two-scale microstructure, Acta Mater. 52 (2004) 631.

[105] M. Wagih, P. Larsen, C. Schuh, Learning grain boundary segregation energy spectra in polycrystals, Nature Commun. 11 (2020) 6376.

[106] A.S. Ebner, S. Jakob, H. Clemens, R. Pippan, V. Maier-Kiener, S. He, W. Ecker, D. Scheiber, V.I. Razumovskiy, Grain boundary segregation in Ni-base alloys: A combined atom probe tomography and first principles study, Acta Mater. 221 (2021) 117354.

[107] M. Wagih, C.A. Schuh, Learning grain-boundary segregation: From first principles to polycrystals, Phys. Rev. Lett. 129 (2022) 046102.